Bilayer Stiffness Identification of Soft Tissues by Suction

N. Connesson[1] · N. Briot[1] · P. Y. Rohan[2] · P. A. Barraud[1] · S. A. Elahi[1] · Y. Payan[1]

Abstract

Background *In vivo* mechanical characterisation of biological soft tissue is challenging, even under moderate quasi-static loading. Clinical application of suction-based methods is hindered by usual assumptions of tissues homogeneity and/or time-consuming acquisitions/postprocessing.

Objective Provide practical and unexpensive suction-based mechanical characterisation of soft tissues considered as bilayered structures. Inverse identification of the bilayers' Young's moduli should be performed in almost real-time.

Methods An original suction system is proposed based on volume measurements. Cyclic partial vacuum is applied under small deformation using suction cups of aperture diameters ranging from 4 to 30 mm. An inverse methodology provides both bilayer elastic stiffnesses, and optionally the upper layer thickness, based on the interpolation of an off-line finite element database. The setup is validated on silicone bilayer phantoms, then tested *in vivo* on the abdomen skin of one healthy volunteer.

Results On bilayer silicone phantoms, Young's moduli identified by suction or uniaxial tension presented a relative difference lower than 10 % (upper layer thickness of 3 mm). Preliminary tests on *in vivo* abdomen tissue provided skin and underlying adipose tissue Young's Moduli at 54 kPa and 4.8 kPa respectively. Inverse identification process was performed in less than one minute.

Conclusions This approach is promising to evaluate elastic moduli *in vivo* at small strain of bilayered tissues.

Keywords Bilayer · Suction · Suction device · Soft tissues characterisation · Experimental mechanics · Inverse identification · Finite elements · Principal component analysis · Skin · Fat · Abdominal tissue

Introduction

Finite element models of soft tissue and organs are widely employed in the field of biomechanics. Such tools help to investigate the underlying mechanisms that either drive normal physiology or contribute to the onset and development of diseases in soft tissues. Finite element models also contribute to the development of medical devices and have the potential to improve computer-assisted medical interventions [1]. Because of large inter-individual variability (both in terms of morphology and in terms of organisation and composition of the tissues), these computational models need to be personalised in order to be clinically relevant. This represents a tremendous challenge because biological tissues exhibit nonlinear, time-dependent, inhomogeneous, and anisotropic behaviours. They also grow, remodel, and adapt to maintain particular mechanical target metrics (*e.g.*, stress).

Extensive work has been conducted for decades in order to characterise the elastic properties of soft tissues. The gold standard for *ex vivo* tissue characterisation are based on conventional mechanical technique such as uni or biaxial tensile tests [2–6], pure shear [3, 7], plain strain compression [3], bulge tests [8, 9], indentation [10, 11] or suction [12]. If such traditional mechanical methods proved invaluable, most of them are destructive (the sample needs to be removed from the body) and cannot be used to characterise the mechanical behaviour *in vivo* (*in situ* analysis). Moreover, several works highlighted the fact that mechanical properties differ significantly between *in vivo* and *ex vivo* conditions (e.g. vascularization of the tissue [13–15], preservation processes [4], *etc*.).

Several attempts were proposed to non-invasively identify mechanical properties of soft tissues *in vivo* [12, 16–21]. Suction-based set-ups, in particular, received a lot of attention for the characterisation of the quasi-static mechanical response of the superficial soft *in vivo* [22]. This technique consists in placing a sterile chamber with an aperture in

✉ N. Connesson
nathanael.connesson@univ-grenoble-alpes.fr

[1] Univ. Grenoble Alpes, CNRS, UMR 5525, VetAgro Sup, Grenoble INP, TIMC, Grenoble 38000, France

[2] Institut de Biomécanique Humaine Georges Charpak, Arts et Métiers Paristech, 151 Boulevard de l'Hôpital, Paris 75013, France

contact with the investigated tissue and decreasing the pressure within the chamber. The amount of tissue aspirated is related to tissue stiffness. The height of the aspirated tissue is generally estimated by ultrasound methods [23–26], mechanical stops [27, 28], optical coherence tomography [26] or cameras usually associated with mirrors or prisms [29–36].

To expand the use of such methods, particular efforts were made to design light devices [28, 37]. Several other developments are necessary to improve the design of the part in contact with the skin so that it becomes unexpensive, disposable, highly adaptive (aperture size, shape, material), and capable of sustaining the required severe sterilisation process. Therefore, our group has been working since 2015 on another approach: replacing the measurement of tissue height with the volume of aspirated tissue [38]. Such a change in the method enabled the elimination of camera, mirror, prism, and all the electronic parts from the system suction head that was basically reduced to a simple tube with an aperture. The corresponding family of devices, called VLASTIC, enabled the evaluation of silicone stiffness with a maximum error of about 10% compared to uniaxial tensile tests [16]. It was also used in a clinical study to evaluate tongue stiffness in ten patients for two conditions: at rest and under general anesthesia [39]. However, in these studies, the underlying tissues were assumed to be homogeneous. The significant differences in the organisation, composition and mechanical behavior of the superficial tissues require a distinction between the different soft tissue layers.

Several attempts have been proposed in the literature for the measurement of the modulus of the top layer(s) of multilayered materials using suction-based techniques. In 2006, Hendriks et al. [26] used suction with 3 aperture diameters (1, 2 and 6 mm) glued to the forearm of a healthy volunteer and imaged by optical coherence tomography. Three FE models were made (one per diameter) which results were compared to experimental data to identify elastic moduli (first order Mooney material behavior) under small deformation of a bilayer model. The upper layer had the thickness of both the epidermis and the papillar dermis (thickness of about 130 μm). The lower layer (thickness of about 1 mm) was the reticular dermis overlying the subcutaneous fat. In this work, the very thin upper layer was surprisingly found about 1500 times softer than the lower layer. In 2011, Zhao et al. [12] demonstrated experimentally and numerically on bilayer gelatin phantoms that a suction diameter smaller than the thickness of the upper layer could be used to characterise only the upper layer elasticity. In Barbarino et al. [40] (2011), the hyperelastic properties of the two first superficial layers of the human face (skin and adipose tissue) were evaluated based on MRI and ultrasound measurements and skin pressure-apex height data. The same team extended this protocol in [36] to identify elastic-viscoplastic material models using different time dependent pressure-apex height curves. In 2021, they also proposed in [41] to identify the properties of each layer of a 5 layer biphasic skin model that would explain a wide range of time dependent *ex vivo* and *in vivo* experimental data. These improvements are very promising but, unfortunately, are difficult to apply in a clinical routine to evaluate patient specific mechanical properties: extensive experimental and numerical work is required for each identification.

In order to address the challenge of developing techniques compatible with the constraints of clinical routine, another approach is suggested: (1) keep the testing system parts in contact with the tissue with the minimum design constraints as possible to favor adaptability, and (2) apply an experimental method as simple and as rapid as possible so that further development could lead to direct clinical application.

By keeping these issues in view, the inverse analyses were also optimised so that identifications can be performed in almost real-time. The associated trade-off is that the material structure and identified mechanical properties need to be simplified. As a first step, only the initial elastic moduli of bilayered structures are sought in this contribution.

This work therefore aims at going beyond the state-of-the-art (i) by using a single, easy to use and adaptable suction system, switching only aperture heads to perform all the measurements, (ii) by proposing identification of Young's moduli of each constituent of bilayered structures using an off-line finite element database in almost real-time, (iii) by evaluating the parameter identifiability of the tested situation.

Additionally, as far as the authors are aware of, only the methods proposed in [12, 28, 31] have been validated on reference phantoms; all other studies directly applied the proposed methods directly *in vivo* to human tissue for which mechanical properties were complex and unknown. Implementing a validation on multi-layered phantoms made from known reference materials is a tedious task that yet seems necessary prior to *in vivo* application. Such comparisons provide realistic error evaluation and confidence in the obtained results.

The whole method of this contribution has been experimentally evaluated by comparing the identified stiffness of bilayer silicone phantoms with classic experimental tensile tests performed on the same material. The method has then been applied *in-vivo* to evaluate the properties of the skin (epidermis and dermis) and fat of the abdomen of a healthy volunteer.

Materials and Methods

The Materials and Methods section is organised as follows: "Cyclic Testing Device to Obtain Pressure-volume Curves" presents the improved cyclic testing device

proposed in this contribution. The device allows to characterise experimentally samples by measuring load-volume curves for different aperture diameters. "Inverse Methodology to Estimate Superficial Bilayer Elastic Stiffness from Pressure-volume Data" presents the inverse methodology implemented to estimate both of the bilayer elastic stiffness, and optionally the upper layer thickness, based on the interpolation of an offline finite element database. The uncertainty evaluation of the identified parameters is also described. "Bilayer Silicone Phantoms", presents the methodology for the fabrication and the mechanical characterisation of custom made bilayered silicone phantoms. Conventional uniaxial tensile test provide reference values to validate the method. "Experimental Protocol for the Suction Device" presents the protocol and the application of the designed device (1) to silicone bilayer phantoms and (2) to the abdomen tissue of a healthy volunteer.

Cyclic Testing Device to Obtain Pressure-volume Curves

Cyclic Testing Device

The testing system was composed of two air-filled parallel circuits both connected at a valve, a manometer (AMS-5812-0015-D-B, Analog Microelectronics GmbH) and a syringe (CODAN 1 mL Luer TBC) (Fig. 1(a)). The stroke ΔL was applied to both syringes simultaneously and cyclically using a loading drawer (Fig. 1(a) and (b)). The volume variation of the syringe $\Delta V_{syringe}$ was supposed to be identical in each circuit (including imperfections such as deformation of the syringe piston, *etc.*).

The first circuit was a simple tube closed at its end, referred to as "Reference circuit". This circuit basically provided a measurement of the volume variation of the syringe $\Delta V_{syringe}$ thanks to the measurement of pressure ΔP_{ref} and a linear model.

$$\Delta V_{syringe} = \frac{\Delta P_{ref}}{k_{ref}} \tag{1}$$

where k_{ref} is the stiffness of the reference circuit. The length of the reference tube was chosen so that the pressure variation ΔP_{ref} in the reference circuit swept the entire sensor pressure range given the input volume variation $\Delta V_{syringe}$.

The second circuit, called the "tissue circuit", was made up of a tube connected to a 3D printed resin cup of suction diameter D_i (Fig. 1(c)) applied onto the tested tissue. A total of $I = 9$ cups, with aperture diameter $D_i \in [4, 30]$ mm, were made in nylon (HP PA11 bio-compatible material) with a HP Multi Jet Fusion 3D printer. All geometric characteristics of the cup in contact with the tested tissue (wall thickness, fillet radius, *etc.*) were proportional to the internal diameter of the aperture D_i. The pressure variation in the tissue circuit is noted ΔP_{tissue}.

The results of these two circuits were combined to provide the global pressure-volume curve $(\Delta P_{tissue\,test} - \Delta V_{syringe\,test})$. The general idea is that this curve can be transformed into the tissue pressure-volume curve $(\Delta P_{tissue\,test} - \Delta V_{tissue\,i})$ [16, 38, 39], where $\Delta V_{tissue\,i}$ is the volume of tissue aspirated into the cup of suction diameter D_i (Fig. 2(a) and (b)).

Taking into account the different volume variations in the tissue circuit between time t_0 and t, it can be written that (Fig. 2(a) and (b)) [39]:

$$\Delta V_{syringe\,test} = \Delta V_{tissue\,i} + \Delta V_{system\,i} \tag{2}$$

where $\Delta V_{system\,i}$ represents both air expansion and system volume variations. Equation (2) means that any additional room $\Delta V_{syringe\,test}$ made into the system thanks to the syringe is filled partly by the aspirated tissue volume $\Delta V_{tissue\,i}$ and partly by the air expansion and system volume reduction $\Delta V_{system\,i}$.

The volume change of the system $\Delta V_{system\,i}$ is a direct function of the pressure inside the tissue circuit. The volume function $\Delta V_{system\,i}$ for each cup of diameter D_i was identified during a separate calibration measurement where the tissue was replaced by an undeformable material (Fig. 2(b), dashed green curve). During calibration, the system volume variation function $\Delta V_{system\,i}$ was directly identified experimentally as equation (2) simplifies into:

$$\Delta V_{syringe\,cal} = \Delta V_{system\,i} \tag{3}$$

Note that the calibration curve $(\Delta P_{tissue\,cal} - \Delta V_{syringe\,cal})$ is different in equation (3) than in equation (2) as the whole tissue circuit is stiffer when testing a non-deformable material than when testing a deformable tissue (Fig. 2(b), green dashed and blue continuous curves, respectively).

In practice, the experimental calibration curve $(\Delta P_{tissue\,cal} - \Delta V_{syringe\,cal})$ for each cup of diameter D_i was approximated by a polynomial of degree 2 to account for small non-linearities in the system.

Measurement of the Reference Circuit Stiffness k_{ref}

The volume $\Delta V_{syringe}$ applied to both circuit was computed using the ΔP_{ref} pressure and the reference circuit stiffness k_{ref} (equation (1)). To evaluate the stiffness of the reference circuit k_{ref}, different cyclic peak-to-peak volume amplitudes ΔV were applied to the reference circuit: the syringe course ΔL was increased step by step by changing the crank eccentricity using a 500 μm thread pitch screw (Fig. 1(b)). The slope of the peak-to-peak pressure

variation amplitude ΔP_{ref} versus the peak-to-peak volume amplitude of $\Delta V_{syringe} = \Delta L\, S_{syringe}$ was considered to be the stiffness of the reference circuit ($k_{ref} = 0.992$ mbar.mm^{-3}).

Inverse Methodology to Estimate Superficial Bilayer Elastic Stiffness From Pressure-volume Data

Let us assume, at this point, that J_i cycles of the tissue pressure-volume curves ($\Delta P_{tissue\,test} - \Delta V_{tissue\,i}$) for each aperture diameter D_i have been measured. Thus, a set of $N_m = \sum_{i=1}^{I} J_i$ curves is available to perform the inverse identification.

Inverse identification consisted in estimating both Young's moduli in the two superficial upper layers (E_{R1} and E_{R0}), and optionally, the thickness L_{R1} of the upper layer (Fig. 3). The physics that explain the dependence of tissue pressure-volume curves ($\Delta P_{tissue\,test} - \Delta V_{tissue\,i}$) on aperture diameter D_i was summarized in "Tissue Volume Normalization and Bilayer Apparent Stiffness B_{ij}". This description lead to the extraction of the apparent stiffness of the bilayer, noted $B_{ij\,EXP}$, from each cycle j of the pressure-volume curves ($\Delta P_{tissue\,test} - \Delta V_{tissue\,i}$).

The N_m experimental apparent stiffnesses $B_{ij\,EXP}$ were then combined with their simulated counterpart to design the cost function Φ_{Param}. This cost function was minimised to identify the parameters in "Noise Model and Cost Function". In this work, the simulated bilayer mechanical apparent stiffnesses were evaluated in real time using interpolated eigen vectors provided by a Principal Component Analysis (PCA) performed over a Finite Element (FE) database. This is similar to the use of pre-calculated abacuses. Details about the used FE model, the associated database, and the eigen vectors provided by the PCA are reported in the Appendix A for clarity and shortening purpose.

Similarly, the mathematical method used to evaluate the uncertainty of the identified parameters and the experimental variance is described in Appendix B.

Tissue Volume Normalization and Bilayer Apparent Stiffness B_{ij}

The pressure-volume curves of the tissue ($\Delta P_{tissue\,test} - \Delta V_{tissue\,i}$) contain information on the mechanical behavior of the tissue integrated over the volume of loaded material below the diameter of the aperture D_i (Fig. 3). As a general rule of thumb, information is extracted up to a depth of about one diameter D_i [12].

On a homogeneous phantom, changing the diameter of the aperture D_i is equivalent to changing the scale of the test, which also changes the volume range in the tissue pressure-volume curves ($\Delta P_{tissue\,test} - \Delta V_{tissue\,i}$). To compare the results obtained with different aperture sizes, the notion of tissue shape S_{tissue} was defined by normalising the volume of the aspirated tissue $V_{tissue\,i}$ by the volume of a half-sphere $V_{ref\,i}$ of diameter D_i [39] (a similar normalisation of the apex height was also found in [12]):

$$S_{tissue} = \frac{V_{tissue\,i}}{V_{ref\,i}} \tag{4}$$

$$\text{with } V_{ref\,i} = \frac{4}{6}\pi\left(\frac{D_i}{2}\right)^3 \tag{5}$$

A shape $S_{tissue} = 1$ means that a volume of half a sphere has been aspirated into the cup, which is the situation illustrated in (Fig. 3(a) and (b)). Note that such a situation was never reached experimentally during this work.

Eventually, the apparent stiffness of the bilayer at diameter D_i and for the loading cycle j was defined as the slope of the cycle j of the curve ($\Delta P_{tissue\,test} - \Delta S_{tissue\,i}$) around a shape $S = 0.1$. This relationship is written as:

$$B_{ij} = \left.\frac{\Delta P_{tissue}}{\Delta S_{tissue\,i}}\right|_{S=0.1} \tag{6}$$

If the material is homogeneous throughout the phantom, the shape pressure curves ($\Delta P_{tissue\,test} - \Delta S_{tissue\,i}$) should overlap for all diameters D_i; the apparent stiffness of the bilayer material B_{ij} should be independent of the suction diameter D_i.

On the contrary, on a bilayered phantom, a change of aperture diameter D_i modifies the relative contribution of the upper layer to the shape S_{tissue} (Fig. 3, change of diameter D_i between situations (a) and (b)); the apparent stiffness of the bilayer material B_{ij} changes with the suction diameter D_i.

In practice, the apparent stiffness of the bilayer material B_{ij} was extracted for each cycle j from the pressure shape curve ($\Delta P_{tissue\,test} - \Delta S_{tissue\,i}$) at a shape $S = 0.1$ by locally fitting a polynomial of degree 1 in the shape range $S \in [0.05, 0.15]$. For a shape of $S = 0.1$, center of the selected range, the material fills only 10% of half a sphere and the whole bilayer material is considered to be loaded under small strains [26].

Noise Model and Cost Function

As the extracted data $B_{ij\,EXP}$ are derivatives, a multiplicative disturbance model was assumed. For each of the N_m measurement point $B_{ij\,EXP}$ with an aperture diameter D_i, it comes:

$$B_{ij\,EXP} = B_{i\,SIM}(\beta, \theta)\ (1 + \epsilon_{ij}) \tag{7}$$

where ϵ_{ij} represents a random disturbance of zero mean and variance σ_i^2. The slope $B_{i\,SIM}(\beta, \theta)$ is the result of the simulation of a suction with a diameter D_i onto a bilayer material. It represents thus the value that would be measured if no

disturbance occurred. The slope $B_{i\,SIM}(\beta,\theta)$ was supposed to present no mismatch with the experimental data once the proper parameter vectors β and θ were found. Moreover, the variance σ_i^2 was supposed to be small compared to one, may depend on the aperture diameter D_i (heteroscedasticity [42, 43]), and must account for both the intra and inter-test variance for diameter D_i. These hypotheses are discussed in "Input Noise Variance Evaluation". The vector β represents the sought unknowns and is of length P. The vector θ represents the other model parameters (aperture diameter D_i, friction, compressibility coefficient, *etc*.). These parameters are described in more details in Appendix A.

The three parameters (the upper layer thickness L_{R_1}, its associated Young modulus E_{R1} and the lower layer Young's modulus E_{R0}, (Fig. 3)) were distributed between the unknowns and model parameters β and θ depending on the identification goals:

$P = 3$ (bilayer, $\beta =< E_{R1}, E_{R0}, L_{R_1} >^T$): when the phantom was a bilayer phantom, the upper layer thickness L_{R_1}, Young's modulus E_{R1} and the lower layer Young's modulus E_{R0} could all be estimated.

$P = 2$ (bilayer, $\beta =< E_{R1}, E_{R0} >^T$): when the phantom was a bilayer phantom, the upper layer thickness might be provided in θ by an annex measurement. In such a case, only the Young moduli of the upper and lower layers E_{R1} and E_{R0} were estimated in β.

$P = 1$ (homogeneous, $\beta =< E_{R1} >$): when the phantom was considered homogeneous, only the averaged material Young's modulus was estimated ($E_{R1} = E_{R0}$). In such a case, the apparent stiffness $B_{i\,SIM}(\beta,\theta)$ is independent of the thickness L_{R_1} of the upper layer.

In practice, the simulated apparent stiffness $B_{i\,SIM}(\beta,\theta)$ was evaluated by interpolating a FE database. This interpolation, based on the eigenvectors provided by a PCA, allowed an evaluation of $B_{i\,SIM}(\beta,\theta)$ in real time. Additional details are reported in Appendix A for clarity and shortening purpose.

With the model proposed in equation (7), the cost function Φ_{Param} was defined in the Weighted Least Square sense (WLS) by comparing the experimental material apparent stiffness $B_{ij\,EXP}$ to its simulated counterpart $B_{i\,SIM}(\beta,\theta)$:

$$\Phi_{Param} = \sum_{i=1}^{I} w_i^2 \sum_{j=1}^{J_i} \left(Ln\big(B_{i\,SIM(\beta,\theta)}\big) + \epsilon_{ij} - Ln\big(B_{ij\,EXP}\big) \right)^2 \tag{8}$$

where I is the number of aperture diameter D_i used, J_i is the number of loading cycle measured for the diameter D_i. Ideally, the weighing factor w_i^2 would be equal to $\frac{1}{\sigma_i^2}$ so that the cost function Φ_{Param} is not dominated by the experimental data provided by a specific aperture diameter D_i [44]. Note that the multiplicative noise model in equation (7) has been converted into an additive noise model in Φ_{Param} using the logarithm function. This method is known as the "both side transformation" method [43], and is also used for inverse identification with suction in [25, 26].

The optimal parameter vector $\widehat{\beta}$ that minimises the cost function Φ_{Param} was estimated by applying the Levenberg-Marquardt method[1] [45] applied to the parameters E_{R1} and L_{R_1} in β. The parameter E_{R0} in β was estimated by solving a linear system since this parameter is linearly conditional on E_{R1} and L_{R_1} (equation (10) Appendix A, please consult [44] for more details). For each identification, different initial guesses were made for the moduli stiffness ratios $\frac{E_{R1}}{E_{R0}}$ [1 2 5 10] and upper layer thickness L_{R_1} [1 4 6 10] mm. Such starting points were tested to avoid possible local minima. In this contribution, the initial guesses had no impact on the identified minimum.

The associated residual norm, noted Φ_0, writes:

$$\Phi_0 = \sum_{i=1}^{I} w_i^2 \sum_{j=1}^{J_i} u_{ij}^2 = \sum_{i=1}^{I} \sum_{j=1}^{J_i} e_{ij}^2 \tag{9}$$

where u_{ij} represents the residual error vector and $e_{ij} = w_i u_{ij}$ is the weighed residual error vector. Note that the residual error vector u_{ij} is slightly different from the noise vector ϵ_{ij} since the noise is also fitted by the model. If the weights w_i^2 were equal to $\frac{1}{\sigma_i^2}$, the residual norm Φ_0 should follow a chi-square distribution with $df = (N_m - P)$ degree of freedom. The rejection threshold at a confidence level of 5% is noted $\chi^2_{df\,95\%}$.

From a statistical point of view, the choice of the weights w_i^2 in the cost function Φ_{Param} does not significantly affect the mean and spread of the identified parameters [43, 46]. In fact, choosing weights w_i^2 representative of the experimental variance σ_i^2 is important mainly if the parameter identifiability is directly inferred from the function Φ_{Param}. This is the case in this contribution. Additionally, a proper evaluation of the experimental variance σ_i^2 is difficult when only few repeatability data is available (which would be the case during a clinical application). In this situation, an idea is to use the residual error vector u_{ij} (equation (9)) to estimate the sought experimental variance σ_i^2. Unfortunately, the initial choice of the weights w_i^2 impacts the identified parameters and residual vector u_{ij}, which, in turn, influences the estimated experimental variance σ_i^2 and its associated weights w_i^2. An iterative procedure was implemented to solve this difficulty, which was possible in this work thanks to the real time evaluation of the simulated apparent stiffness

[1] *lsqnonlin* function in MATLAB

$B_{i\,SIM}(\beta, \theta)$. For concision purpose, the mathematical methods applied to evaluate the parameter identifiability and the variance estimation derived from the residual vector u_{ij} are reported in Appendix B.

Bilayer silicone phantoms

To validate the method, bilayered phantoms were made of two mechanically characterised silicones R_0 (soft) and R_1 (stiffer).

These silicones were obtained by mixing equal mass of component A and B[2] and adding silicone softener[3] (14.6% of $(A+B)$ mass for R_1, 30% of $(A+B)$ mass for R_0). The mixed silicones were vacuumed during 5 min to remove air bubbles prior to pouring.

Three types of phantoms were made:

Homogeneous Suction Phantoms : simple cylinders of ∅96 mm × 70 mm used as references and labelled R_0 and R_1 (Fig. 4(a)).

Bilayered Suction Phantoms : cylinders of ∅96 mm, with thick R_0 bottom layer (soft), and thin upper R_1 layer (stiffer) of thickness L_{R_1} (A to E, Fig. 4(a)). The phantoms were made upside down: the R_1 stiffer layer was first moulded by controlling the volume poured with a syringe, followed one hour later by the softer layer of R_0.

Flat tensile specimens : 5 to 10 flat specimens ($40 \times 160 \times 3$ mm^3 molds) were moulded from the same mixes as the suction phantoms. The average section A_0 of these specimens were estimated by weighting each specimen mass m_{tens} so that $m_{tens} = \rho\, b\, A_0$ with ρ the silicone volumetric mass and b the length of the mould.

The reference silicone tensile Young's Moduli $E_{R1\,tens}$ and $E_{R0\,tens}$ were evaluated during quasi-static uniaxial tensile tests on a MTS tensile machine.

Experimental Protocol for the Suction Device

The proposed suction-based methodology for the mechanical characterisation of superficial layers was applied (1) on silicone bilayer phantoms and (2) to the abdomen tissue of a healthy volunteer (4 cm to the right of the umbilical cord).

Ethical agreement for study participant: a 38 year-old male healthy volunteer, with a body mass index of 25.4, was included in this preliminar study. He gave his informed consent to the experimental protocol previously approved by the local ethics committee (study agreement CERNI N° 2013-11-19-30) and as required by the Declaration of Helsinki (1964).

Sampling frequency: the pressures in the reference and tissue circuits $(\Delta P_{tissue} - \Delta P_{ref})_n$ were measured simultaneously. The underscript n represents the measurement index. The pressure sampling frequency was of 100 Hz. The pressures of the two circuits were synchronised once per cycle using a homing sensor (Fig. 1(b)).

Cyclic volume amplitude: the peak to peak volume $\Delta V_{syringe}$ amplitude was of 0.1 mL and kept identical for all cup diameters D_i. Note that with such a small withdrawn volume, testing the system *in-vivo* presents absolutely no risk to the subject. A complete cycle (withdrawal and injection) lasted about 10 seconds. Only pressure signals obtained during withdrawing and for $\Delta V_{syringe} > 0.01$ mL were used to avoid impact of possible syringe piston asymmetrical behaviour during movement inversion in the reference and tissue circuits. For the *in-vivo* measurements, the volunteer was also asked to hold his breath during withdrawal.

Inter and intra test reproducibility: on the silicone phantoms, a total of 5 cycles were performed during each acquisition (intra-test reproducibility). Each test has been performed 2 to 3 times (inter-test reproducibility). On the abdomen, a total of 10 cycles were performed during each acquisition (intra-test reproducibility). Each test has been performed 5 to 7 times (inter-test reproducibility).

Circuit air-tightness and initial air quantity: during calibration or measurement on tissues, an ultrasound gel cord filled an external groove to ensure air tightness (Fig. 1(a)). Pressure-pressure curves $(\Delta P_{tissue} - \Delta P_{ref})_n$ were monitored during all tests; leakage was identified when pressure P_{tissue} drifted cycle after cycle. Such tests were immediately discarded.

The air quantity enclosed in the system during the calibration and measurement on tissues should be identical to obtain correct mechanical characterizations. To achieve this, the syringes were set in their empty reference position using the homing sensor (Fig. 1(b)) before closing the valves: the air volume enclosed in the system was reproducible and minimum at the starting point ($n = 0$). Note that during *in-vivo* tests on the abdomen tissue, the cup was placed in position about 2 minutes before performing the first test so that the aperture temperature was stable during the test.

Diameter order: during *in-vivo* tests on the abdomen tissue, the measurements were performed with increasing cup sizes (4 mm to 30 mm).

Normal loading minimisation: each aperture is connected to a tube and is held in place on the tissue during a test, which necessarily adds normal and shear loads between the aperture and the tissue. In any situation, these loads were kept as low as possible without impacting the circuit air-tightness.

[2] Two main components of Skin FX10 110019

[3] Deadner Skin FX10 110020

When a measurement was made on a silicone phantom, a special 3D printed[4] holder (Fig. 4(a), applied to phantom *A*) was used to hold the cup in place. The aim of this holder is to minimise the influence of the tube and to minimise as much as possible the normal and shear loads between the aperture and the phantom.

During tests on abdominal tissue, the cups were held with a medical plaster placed on one side of the cups for diameters smaller than $D_i = 15$ mm. For larger diameters, no plaster was applied as the ultrasound gel cord and cup weight were enough to ensure air-tightness.

During calibration, the cup D_i was placed on an underformable material (2 mm sheet of vulcanised rubber glued to an aluminium block) and held in place with a clamp.

Upper layer thickness measurement: on the silicone phantoms, destructive measurements were performed after suction tests: all phantoms were cut in half. Each upper layer was peeled off; the separation naturally occurred at the interface between R_1 and R_0. Magnified scaled control pictures were then taken with a camera. The thickness were evaluated at 8 different locations.

The abdomen tissue has been considered as a bilayer, namely the upper layer composed of the epidermis and dermis, and the lower layer composed of fat and muscle. The thickness of the upper layer was evaluated using eight Bmode UltraSound (US) local measurements[5]. Fat and muscle thicknesses were measured using the same method but with a different probe[6].

Results

Reference Values Obtained on Phantoms

The tensile results obtained on R_0 and R_1 flat silicone specimens are presented in Fig. 4(b). Fitting a Neo-Hookean incompressible model onto the tensile curves for $\lambda_1 = \frac{L}{L_0} \in [1, 1.1]$ provided Young's moduli of $E_{R1\,tensile} = 74.7 \pm 2.3$ kPa and $E_{R0\,tensile} = 8.97 \pm 0.64$ kPa where the tolerance intervals are given as twice the experimental standard deviation (Table 1).

The stiffness ratio $\frac{E_{R1\,tensile}}{E_{R0\,tensile}}$ observed using tensile data is equal to 8.3.

The optically measured thickness $L_{R_1\,pic}$ of reference bilayer phantoms are presented in Table 2. Errors intervals are given as twice the experimental standard deviation. The thickness results using Bmode US on abdomen tissue (Fig. 5(a) and (b)) are also reported in this table.

[4] 3D printer Prusa MK3S+

[5] Aixplorer, probe SuperLinear™ SLH20-6

[6] Aixplorer, probe SuperLinear™ SL10-2

Table 1 Reference values: identified Young's Moduli from tensile test on flat specimens. The reported Confidence Intervals (CIs) are twice the identification standard deviation

Flat tensile specimens	$E_{tensile}$ (kPa)	CI at 95% (kPa)
R_0	**9.0**	±0.65
R_1	**74.7**	±2.3

Tissue Pressure-volume Curve: ($\Delta P_{tissue\,test} - \Delta V_{tissue\,i}$)

Illustrations of the experimental tissue pressure-volume curves ($\Delta P_{tissue\,test} - \Delta V_{tissue\,i}$) are presented for the phantom *A* and on the abdomen tissue with the different aperture diameters D_i in Figs. 6(a) and 7(a) respectively. Only the first cycle for the first test is presented. The data selected to compute the apparent material stiffness $B_{ij\,exp}$ is presented in colour on the plots (the shape range the closest possible to $S \in [0.05, 0.15]$). The apparent stiffness $B_{ij\,exp}$ of phantom *A* and on the abdomen tissue are presented in colour in Figs. 6(b) and 7(b), respectively. The results $B_{ij\,exp}$ for all cycles of all tests are also presented as black markers in these plots. Note that the results $B_{ij\,exp}$ are randomly distributed around the first cycle result (coloured marker, Fig. 7(b)); the cyclic loading history did not have any visible impact on the experimental results for the applied shape range when testing the abdomen tissue.

Table 2 Reference values: layer thickness $L_{R_1\,pic}$ evaluated by an annex destructive measurement on silicone phantoms. Measurement $L_{skin\,US}$ using Bmode ultrasound with two different probes on the abdomen. The reported Confidence Intervals (CIs) are twice the experimental standard deviation

Suction specimen	Layer thickness $L_{R_1\,pic}$ or $L_{skin\,US}$ (mm)	CI at % 95 (mm)
R_0	0	
A	1.08	±0.064
B	3.27	±0.06
C	6.22	±0.055
D	9.16	±0.076
E	11.75	±0.05
R_1	69	
Abdomen {epidermis + dermis}	2.21	±0.033
Abdomen fat	22 to 27	
Abdomen muscle	about 12.5	

Table 3 Identification results from suction data on homogeneous phantoms for the $P = 1$-parameter model

	Suction phantom	$\Phi_0/\chi^2_{df\,95\%}$	E_{opt} (kPa)	RE (%)	CI at 95% (kPa)
Model $P = 1$	$R0$	318/175	**10.9**	(*21.1%*)	±0.12
Model $P = 1$	$R1$	7/127	**81.2**	(*8.6%*)	±1.07

Material Apparent Stiffness: $B_{ij\,exp}$

The experimental material apparent stiffness $B_{ij\,exp}$ (equation (6)) for each cycle and for all the silicone phantoms are presented as a function of the aperture diameter D_i in Fig. 8(a). Taking advantage that the thicknesses $L_{R1\,pic}$ were measured during an annex measurement (Table 2), the experimental apparent stiffness $B_{ij\,exp}$ are also plotted versus the scale ratio $\frac{D_i}{L_{R1\,pic}}$ in Fig. 8(b).

Experimental Variances σ_i^2

The variances of the experimental data were evaluated over the logarithm of the material apparent stiffness $Ln(B_{ij\,k})$ (equations (15) and (16), Appendix B). The variances on silicone phantoms and during *in vivo* tests were evaluated separately.

To compute $\sigma^2_{i\,AUE}$ (equation (16), Appendix B), all experimental data were used (671 data points $B_{ij\,EXP\,k}$ for the silicone phantoms, 560 data points for the abdomen tissue).

Silicone Phantoms

A model with $P = 2$ was applied to each phantom A to E. A model with $P = 1$ was applied to phantoms R_0 and R_1. The weights w_i, initially chosen equal to one, were updated at each iteration until the convergence of the AUE variance estimation. The sought Young's moduli $\beta =< E_{R1}, E_{R0} >^T$ were shared between the models so that the optimal moduli was the unique

Table 4 Identification results for the $P = 2$ and $P = 3$-parameter models on the silicone phantom: the optimal identified values are in **bold**. The Relative Errors (RE) between optimal suction and tensile reference values are in (*italic*). The confidence interval provided was computed at 95% for each parameter. Color code: light gray if $|RE| < 15\%$, gray if $15\% < |RE| < 30\%$, darker gray if $|RE| > 30\%$

Model $P = 2$				
phantom	$\Phi_0/\chi^2_{df\,95\%}$	$L_{R_1\,pic}$ (mm)	$E_{R_1\,opt}$ (kPa)	$E_{R_0\,opt}$ (kPa)
A	15/129.9	1.08 ± 0.064	**91.3** (*22%*) ±16.9	**9.6** (*7%*) ±0.35
B	13/121	3.27 ± 0.06	**81** (*8%*) ±4.5	**9.9** (*11%*) ±0.5
C	6/135.5	6.22 ± 0.055	**82.9** (*11%*) ±2.6	**12.3** (*38%*) ±1.25
D	16/146.6	9.16 ± 0.076	**82.5** (*10%*) ±2.1	**12.6** (*40%*) ±2.25
E	7/152.1	11.75 ± 0.05	**82.2** (*10%*) ±2	**11.4** (*27%*) ±4

Model $P = 3$				
phantom	$\Phi_0/\chi^2_{df\,95\%}$	$L_{R_1\,opt}$ (mm)	$E_{R_1\,opt}$ (kPa)	$E_{R_0\,opt}$ (kPa)
A	13/128.8	**1.41** (*30%*) ±0.45	**60.9** (*-19%*) ±27	**9.4** (*5%*) ±0.4
B	11/119.9	**3.04** (*-7%*) ±0.33	**87.5** (*17%*) ±11.1	**10.3** (*15%*) ±0.7
C	3/134.4	**5.46** (*-12%*) ±0.73	**86.9** (*16%*) ±5.25	**15.5** (*72%*) ±3.15
D	15/145.5	**7.89** (*-14%*) ±2.1	**84.4** (*13%*) ±4	**19** (*111%*) ±10.8
E	4/151	**7.86** (*-33%*) ±3.71	**85.2** (*14%*) ±4.25	**31.8** (*254%*) ±19.6
$R0$	50/173	**0.34** (*N.A.*) ±1.23	**178.9** (*N.A.*) ±1320	**9.1** (*2%*) ±0.85
$R1$	-	Not converged	Not converged	Not converged

Table 5 Identification results for the $P = 2$ and $P = 3$-parameter models on the abdomen tissue: the optimal value is in **bold**. The Relative Error (RE) between reference and optimal suction thickness is in (*italic*). The confidence interval provided were computed at 95% for each parameter

Abdomen tissue results	$\Phi_0/\chi^2_{df\,95\%}$	$L_{skin\,US}$ or $L_{skin\,opt}$ (mm)	$E_{skin\,opt}$ (kPa)	$E_{fat\,opt}$ (kPa)
Model $P = 2$	558/614	2.21±0.033	**53.5** ±1.05	**4.8** ±0.1
Model $P = 3$	553/613	**2.15** (*-3%*) ±0.05	**54.9** ±1.35	**4.9** ±0.1

set noted $E_{R1\,all} = 84.40$ kPa and $E_{R0\,all} = 9.85$ kPa (Fig. 9(a) and (b), each black curve being computed with the layer thickness $L_{R1\,pic}$ of the considered phantom (Table 2)). The resulting stiffness ratio is $\frac{E_{R1\,all}}{E_{R0\,all}} = 8.56$.

After the convergence of the weights w_i^2, the norm of the residual error vector was $\Phi_0 = 669.16$. The residual error Φ_0 should follow a chi-square probability law with $df = (N_{ki} - P) = 669$ degree of freedom. For such a chi-square law, the acceptability threshold at $\alpha = 5\%$ is $\chi^2_{df\,95\%} = 730$.

The residual error vector u_{ijk} used to compute the converged σ^2_{iAUE} (equation (16), Appendix B) is presented in Fig. 9(c). The final values of σ^2_{iAUE} are presented in Fig. 9(d). Variances $\sigma^2_{iClassic}$ (equation (15), Appendix B) are also presented in Fig. 9(d). For these measurements on silicone phantom, heteroscedacity is clearly visible, the logarithmic both-side transformation being insufficient to remove it completely.

Table 6 Young's moduli reported in literature for human 'skin' tissue and low deformation. Equivalent Young's moduli are derived from the mechanical parameter reported in each reference, and considering incompressible materials when performing conversions under small deformation ($E = 3\mu$ where μ is the reported shear modulus, $E = 6C_{10}$ where C_{10} is the classic material parameter used in strain energy function based on the first invariant of the Finger strain tensor, *etc.*). The similarities between this contribution and literature are represented with gray colour. *In*=*In Vivo*, *Ex*=*Ex Vivo*, Abd=Abdomen, Tho=Thoracic, FA=ForArm, Indent=Indentation. When using suction, the number of diameters D_i and range in mm are reported in comments along with measurement techniques (Vol=Volume, US=Ultrasounds, Cam=Camera, Stop=Mechanical stop)

'Skin'	Ref	*In*/*Ex vivo*	Site	Thickness (mm)	Method	Comment	Elastic modulus (kPa)	Age
Connesson 2022		*In*	Abd	2.15 – 2.21	Suction	$9D_i[4-30]$, Vol	54 ± 1	38
Jansen 1958	[52]	*Ex*	Abd	0.9-1.9	Tension	$\sigma \in [0\ 490]$ kPa	1080 – 2 160	0 – 90
Silver 2001	[53, 54]	*Ex*	Abd/Tho	–	Tension	$\lambda_1 \in [1\ 1.4]$	100	47 – 86
Diab 2019	[9]	*Ex*	Abd	2.9 – 4	Bulge	Lanir model	0.6 – 7.5	51 – 65
Annaidh 2012	[55]	*Ex*	Back	1.78 – 3.34	Tensile		540 – 1 950	81 – 97
Tongue 2013	[8, 56]	*Ex*	Back	2 – 4.8	Bulge		14.3 – 67.9	43 – 83
Diridollou 2000	[24]	*In*	FA	0.9 – 0.95	Suction	$1D_i[6]$, US	41 – 217	20 – 30
Hendriks 2003	[25]	*In*	FA	1.21 – 1.51	Suction	$1D_i[6]$, US	29 – 102	19 – 24
Barel 2006	[57]	*In*	Various	–	Suction	$1D_i[2]$, Cam	130 – 260	-
Barbarino 2011	[40]	*In*	Face	1.6 – 1.8	Suction	$2D_i[2, 8]$, Cam	19 – 25	30
Weickenmeier 2015	[33]	*In*	Face	1.7	Suction	$2D_i[2, 8]$, Cam	6.96	29
Muller 2020	[28, 58]	*In*	Divers	1.2	Suction	$1D_i[6]$, Stop	6.9 – 17.42	-
Lakhani 2021	[36]	*In*	FA	1.1 – 1.25	Suction	$1D_i[30]$, Cam	520 – 590	31 – 36
Agache 1980	[59]	*In*	FA	1 for all	Torsion	Torque imposed	420 – 850	3 – 89
Khatyr 2004	[60]	*In*	FA	–	Tension		130 – 660	22 – 68
Pailler-Mattei 2008	[61]	*In*	FA	1.2	Indent		4.5 – 8	30
Zahouani 2009	[62]	*In*	Arm	–	Indent		2.1 – 6.2	55 – 70
Jackowitcz 2007	[63]	*In*	Face/FA	1.5	Indent		7 – 33	28 – 65

Table 7 Young's moduli reported in literature for human fat/adipose tissue. SMAS=Superficial Muscular Aponeurotic System, *In*=*In Vivo*, *Ex*=*Ex Vivo*, SupF=Superficial Fat, MRE= Magnetic Resonance Elastography. When using suction, the number of diameters D_i and range (in mm) are reported along with measurement techniques (Vol=Volume, Stop=Mechanical stop, Cam=Camera, US=Ultrasounds)

'Fat'	Ref	Type	Site	Label	Method	Comment	Elastic modulus (kPa)
Connesson 2022		*In*	Abd	Adipose	Suction	$9D_i[4-30]$ Vol	4.8 ± 0.1
Patel 2005 [64]		*Ex*	Abd	Adipose	Torsion	Strain 1%, $f = 3$ Hz	$3.9 - 6$
Sommer 2013 [65, 66]		*Ex*	Abd	Fat	Multiaxial	Fitted in [66]	0.79
Hendriks 2003 [25]		*In*	FA	Fat	Suction	$1D_i[6]$, US	0.12
Barbarino 2011 [40]		*In*	Face	SMAS + SupF	Suction	$2D_i[2, 8]$ Cam	$2.4 - 3.87$
Weickenmeier 2015 [33]		*In*	Face	SMAS	Suction	$2D_i[2, 8]$ Cam	0.17
Muller 2018 [58]		*In*	Divers	Subcutaneous	Suction	1D(6) Stop	0.084
Weaver 2005 [67]		*In*	Foot	Fat pad	MRE		$22.5 - 29.2$
Pailler-Mattei 2008 [61]		*In*	FA	Hypodermis	Indent		2
Lawrence 1998 [68]		*In*	Breast	Fat	MRE	$f = 50 - 100$ Hz	$0.87 - 1.71$
McKnight 2002 [69]		*In*	Breast	Adipose tissue	MRE	$f = 100$ Hz	$2.8 - 17$
Lorenzen 2002 [70]		*In*	Breast	Fatty tissue	MRE	$f = 65$ Hz	$0.5 - 4$
Van Houten 2003 [71]		*In*	Breast	Fat	MRE		$14 - 27$
O'Hagan 2009 [72]		*Ex*	Breast	Fat necrosis	Indent		4.2
Samani 2004 [73]		*Ex*	Breast	Adipose tissue	Indent		$1.5 - 2.2$
Samani 2007 [10]		*Ex*	Breast	Normal Fat	Indent		$1.43 - 5$

Abdomen Tissue

A model with $P = 2$ was identified on the abdomen data while updating the weights w_i, initially chosen equal to one, at each iteration. The residual converged error vector u_{ij} used to calculate σ^2_{iAUE} (equation (16), Appendix B) is presented in Fig. 11(c). The final values of σ^2_{iAUE} are presented in Fig. 11(d). Variances $\sigma^2_{iClassic}$ (equation (15), Appendix B) are also presented in Fig. 11(d).

The norm of the residual error vector was $\Phi_0 = 558$. The residual error Φ_0 should follow a chi-square probability law with $df = (N_{ki} - P) = 558$ degree of freedom. For such a chi-square law, the acceptability threshold at $\alpha = 5\%$ is of $\chi^2_{df\,95\%} = 614$.

Optimal Parameter β and Identifiability

For all the identifications presented hereafter, the variances σ^2_{iAUE} have been used to compute the weights w_i^2 in equation (8).

For illustration purpose, details of fitted curves, Indifference Regions (IR) and Confidence Intervals (CIs) are presented on the phantom *B* and on the abdomen tissue (Figs. 10 and 11). The suction results obtained on phantoms R_0 and R_1 for $P = 1$ are summarised in Table 3 with direct comparisons to the tensile reference values.

The results of the suction on silicone phantoms *A* to *E* are summarised in Table 4 for $P = 2$ and 3 with direct comparisons to the reference values when applicable.

Note that, on the stiffer silicone R_1, the measurement $B_{ij\,exp}$ is almost independent on the aperture diameter D_i (Fig. 8(a), red curve) which is in accordance with theory for a upper layer thickness greater or equal to the aperture diameters [12]. The suction test overestimated the R_1 Young's Modulus compared to the tensile result $E_{R1\,tensile}$ by 8.6% (Table 3). On the softer silicone R_0, the measurement $B_{ij\,exp}$ increased for small D_i (Fig. 8(a), blue lowest curve). This behaviour was not expected for an homogeneous phantom. A possible explanation is that soft materials are very sensitive to normal loading applied to small cups [28]. Such an initial load causes the material surface to be curvaceous, which replaces some air into the cup by material before closing the system valve. The calibration curve used, measured on a flat undeformable surface, is thus less stiff than reality. This bias induces an underestimation of the tissue volume $\Delta V_{tissue\,i}$ and an overestimation

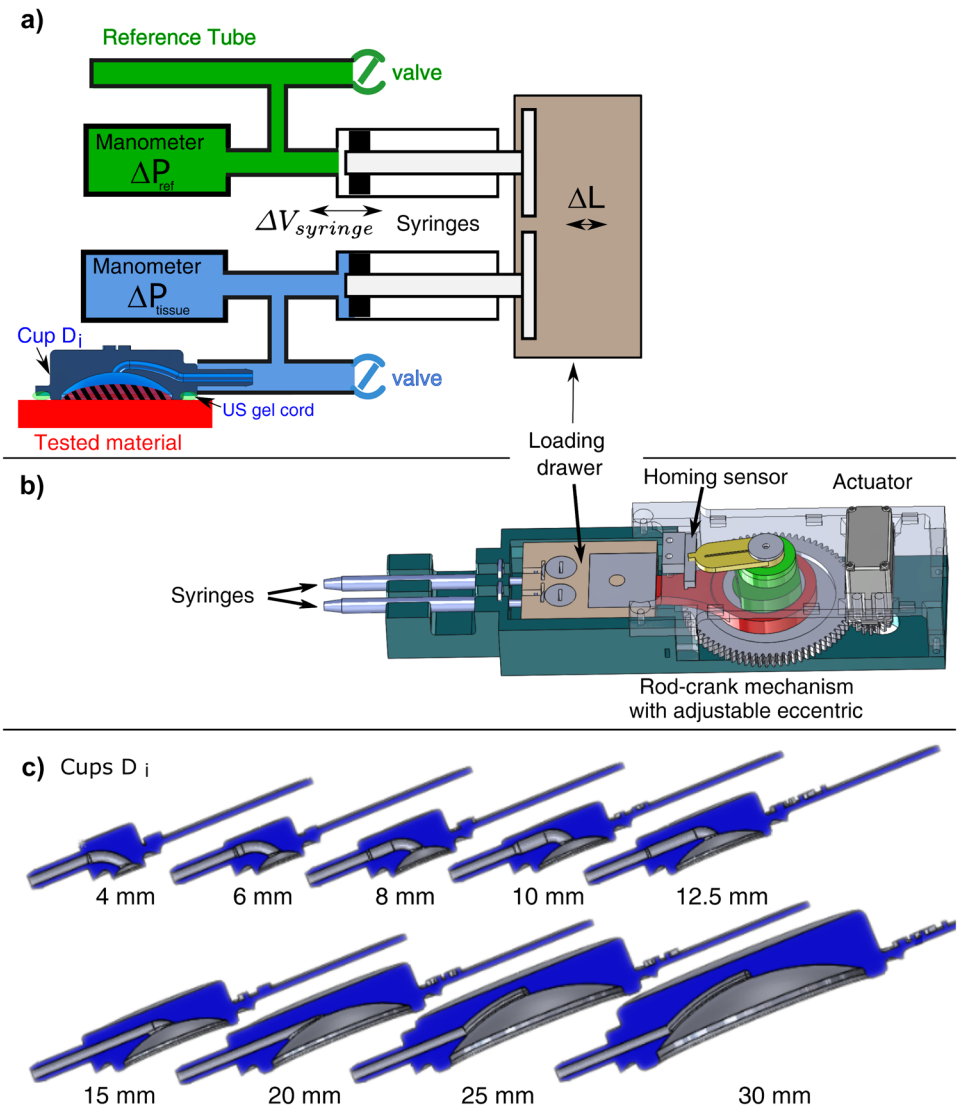

Fig. 1 **Subplot** (**a**) Principle of the two circuits system to evaluate the material mechanical answer of soft tissues during cyclic suction. **Subplot** (**b**) Syringes cyclic actuator with adjustable screw-driven eccentric and homing sensor. **Subplot** (**c**) Suction cups with aperture diameters ranging from 4 to 30 mm

of measurement $B_{ij\,exp}$. However, this phenomenon should be limited by the presence of the holding system (Fig. 4(a)). In any case, this experimental result causes the $P = 1$-parameter model to overestimate the R_0 Young's Modulus compared to the tensile one $E_{R0\,tensile}$ by 21.1%. The fitting score of $\Phi_0 = 318$ is above the threshold value of $\chi^2_{df\,95\%} = 175$ (Table 3); this curve could be considered as an outlier.

Also note that phantom *A* had a very thin upper layer of 1.08 mm: the aperture diameters from 4 to 30 mm were well adapted only to extract information about the stiffness E_{R_0} of the lower layer. Relative errors with tensile test on soft silicone E_{R_0} were lower than 10% (7 and 5% for $P = 2$ or $P = 3$-parameter models, respectively, Table 4). The smallest aperture diameter being 4 times larger than the thickness of the upper layer, the upper modulus E_{R1} is the least well identified among the silicone phantom tested (relative error of +22 and −19% for $P = 2$ or $P = 3$-parameter models, respectively, Table 4), which is pointed out by the suction indifference region greater than 17 kPa on E_{R_1}.

Phantom *B*, with an upper layer of 3.27 mm is the most adapted among the phantoms to provide both proper upper and lower layer moduli given the used aperture diameters range ($|RE| < 15\%$ for all optimal values and for $P = 2$, and close to 15% for the $P = 3$-parameter models, Table 4).

Phantoms *C* to *E*, with layers thicker than 6 mm, provide only proper upper layer modulus E_{R1} identification (RE lower than 15%).

A more global summary on silicone phantoms is graphically represented in Fig. 12 to show the CI variations with the value of parameter *P* and the upper layer thickness. The results obtained on homogeneous phantoms ($P = 1$) and by tensile tests are reported as horizontal red, blue and black bands of twice the experimental Std (indifference regions at 95%).

The aspiration results on the abdomen tissue are summarised in Table 5 for $P = 2$ and 3.

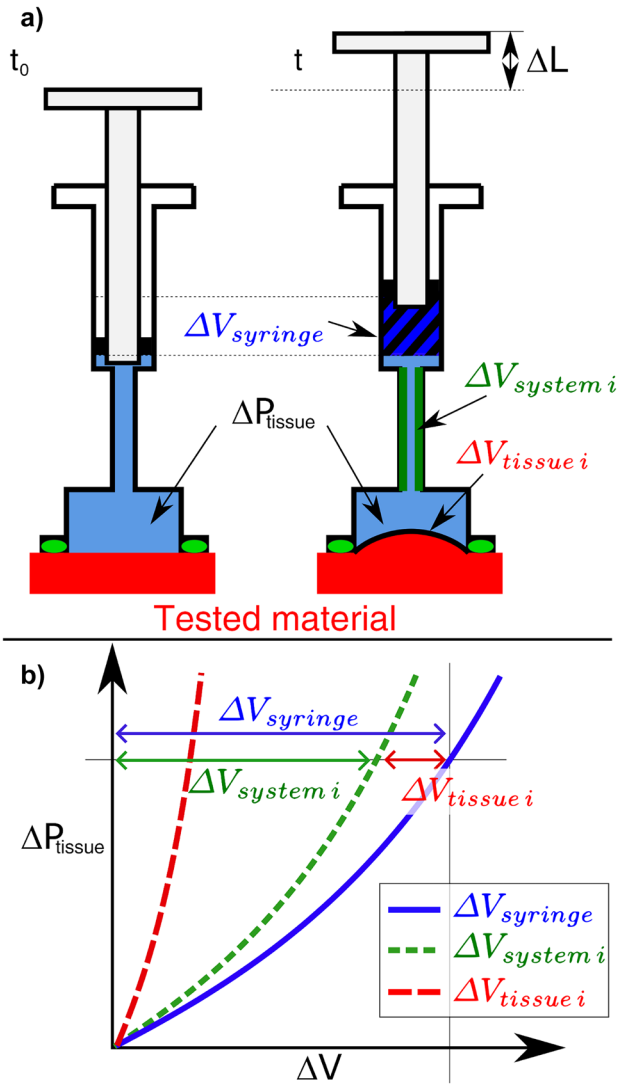

Fig. 2 **Subplot** (**a**) Schematic of the tissue circuit at the initial time t_0 and t: definition of volumes $\Delta V_{tissue\,i}$, $\Delta V_{syringe}$ and $\Delta V_{system\,i}$. The room $\Delta V_{syringe\,test}$ made into the system thanks to the syringe is filled in part by the volume of aspirated tissue $\Delta V_{tissue\,i}$ and in part by the expansion of the air and the reduction of the volume of the system $\Delta V_{system\,i}$. **Subplot** (**b**) Schematic pressure-volume curves during calibration measurement (green dashed curve) or with a soft tissue tested (blue continuous curve). The tissue pressure-volume curve is the difference between the total and calibration curves at the same pressure (red dashed curve)

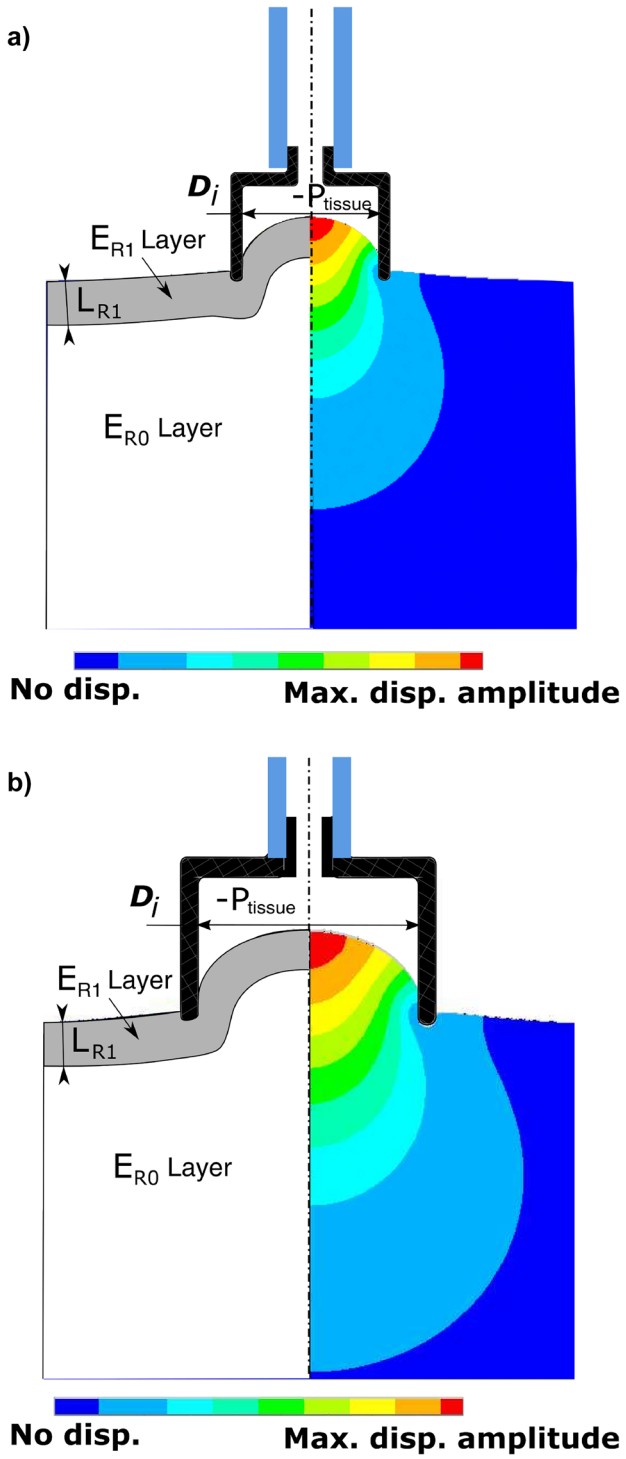

Fig. 3 Illustration of suction on a bilayer phantom using different aperture diameters for $S_{tissue} = 1$. The colours under the cups schematically represent the material volume over which the material stiffness information is extracted. Changing the suction diameter D_i modifies the relative contribution of the upper layer to the final shape S_{tissue} (Subplots (**a**) to (**b**))

Discussion

The aim of this work was to improve *in vivo* suction-based mechanical characterisation of the superficial layers of soft tissues. To go beyond the state-of-the-art, an adaptable suction system was proposed in this contribution, allowing to perform suction tests with multiple aperture diameters.

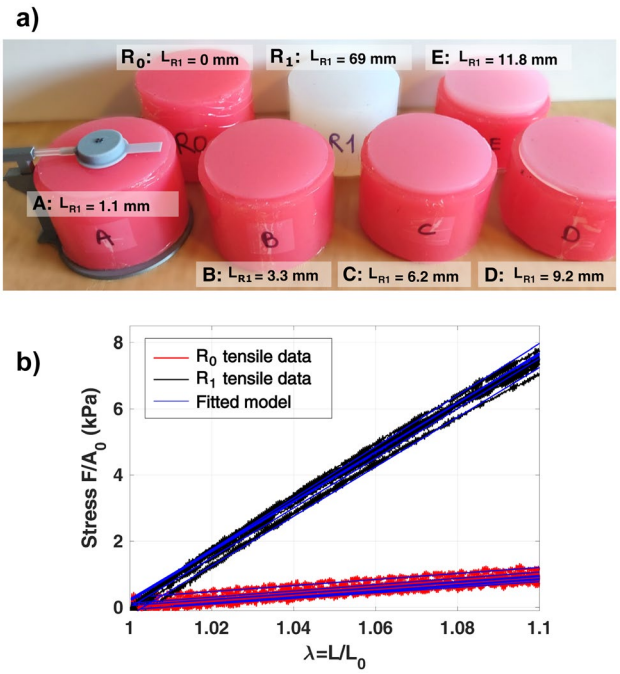

Fig. 4 **Subplot** (**a**) Homogeneous (R_0 and R_1) and bilayered suction phantoms (A to E) made with stiffer R_1 silicone as upper layer (white) and softer R_0 silicone as bottom layer (pink). **Subplot** (**b**) Tensile test results on flat rectangular specimens ($40 \times 160 \times 3\ mm^3$). Softer R_0 silicone (red curve) and stiffer R_1 silicone (black curve). Associated Neo-Hookean curve fitting (blue) using data over the domain for $\lambda_1 = \frac{L}{L_0} \in [1, 1.1]$

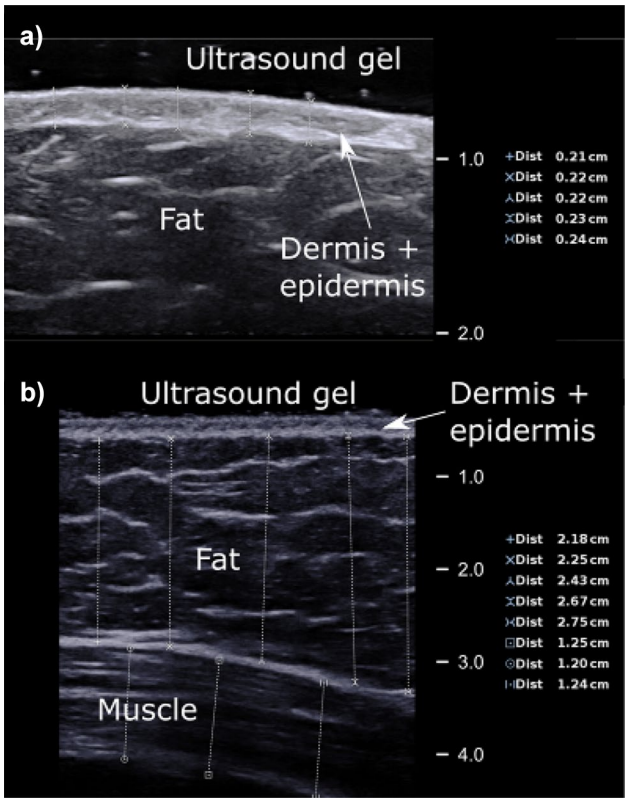

Fig. 5 **Subplot** (**a**) Illustration of Bmode imaging on the upper structures of the abdomen tissue of the volunteer (Aixplorer, probe SuperLinear™ SLH20-6). From top to bottom, the ultrasound gel is first visible in black (no direct contact between the probe and the skin), then the dermis and epidermis are visible in white, and then the fat underneath. The upper layer thickness is measured directly using the firm ultrasound software. **Subplot** (**a**) Illustration of Bmode imaging on fat and muscle of the abdomen tissue of the volunteer (Aixplorer, probe SuperLinear™ SL10-2). From top to bottom, the ultrasound gel is first visible in black, then the dermis and epidermis in white, then fat and muscle underneath

Inverse identification of Young's moduli of a bilayered structure was performed in less than one minute per phantom using an offline finite element database. Representative confidence intervals were also provided.

The method was successfully tested on controlled bilayer phantoms for upper layer thickness from 1 to 12 mm. The bilayer phantom with an upper layer of 3 mm presented the best parameter identifiability for both Young's moduli (relative errors lower than 10% compared to reference values obtained during tensile tests, which is of the same order of magnitude as in [16] on homogeneous material). To the authors' knowledge, no other published results are available in the literature to compare identified moduli onto bilayer materials to tensile values on the same material.

The proposed method is expected to hold for any other stiffness ratios, even if, in this contribution, only two controlled silicone mixes R_1 and R_0 were used experimentally; the stiffness ratio $\frac{E_{R1}}{E_{R0}} \approx 8.3$ was identical for all suction phantoms A to E, which corresponds to a unique curve of the FE database (equation (10), Appendix A). The experimental curves overlap in the plot of $B_{ij\,exp}$ versus the ratio $\frac{D_i}{L_{R1\,pic}}$ (Fig. 8(b)) confirms that this uniqueness of stiffness ratio is actually observed experimentally with the suction tests; this is a qualitative assessment of the measurement quality of both $B_{ij\,exp}$ and $L_{R1\,pic}$. Depending on the layer thickness L_{R1}, the aperture diameters from 4 to 30 mm extract different parts of the total theoretical curve (Fig. 8(a) and (b)).

The method has also been successfully applied *in vivo* to the abdominal tissue of a healthy volunteer. Young's moduli identified on the skin (dermis and epidermis) and on the subcutaneous fat were of 54 ± 1 kPa and 4.8 ± 0.1 kPa, respectively (stiffness ratio $\eta = \frac{E_{skin}}{E_{fat}} = 11.25$). Seven main points are discussed before comparing these results with the literature.

First, the *in-vivo* tissue pressure-volume curves show almost linear behaviour (Fig. 7(a)) and no loading history dependence (Fig. 7(b)) for shapes S_{tissue} smaller than 0.1. The similarities between the tissue and silicone phantom pressure-volume curves are striking (Figs. 6 and 7(a)). Therefore, it is assumed that the method remains valid (as demonstrated on the silicone phantoms) for these *in-vivo* tissues.

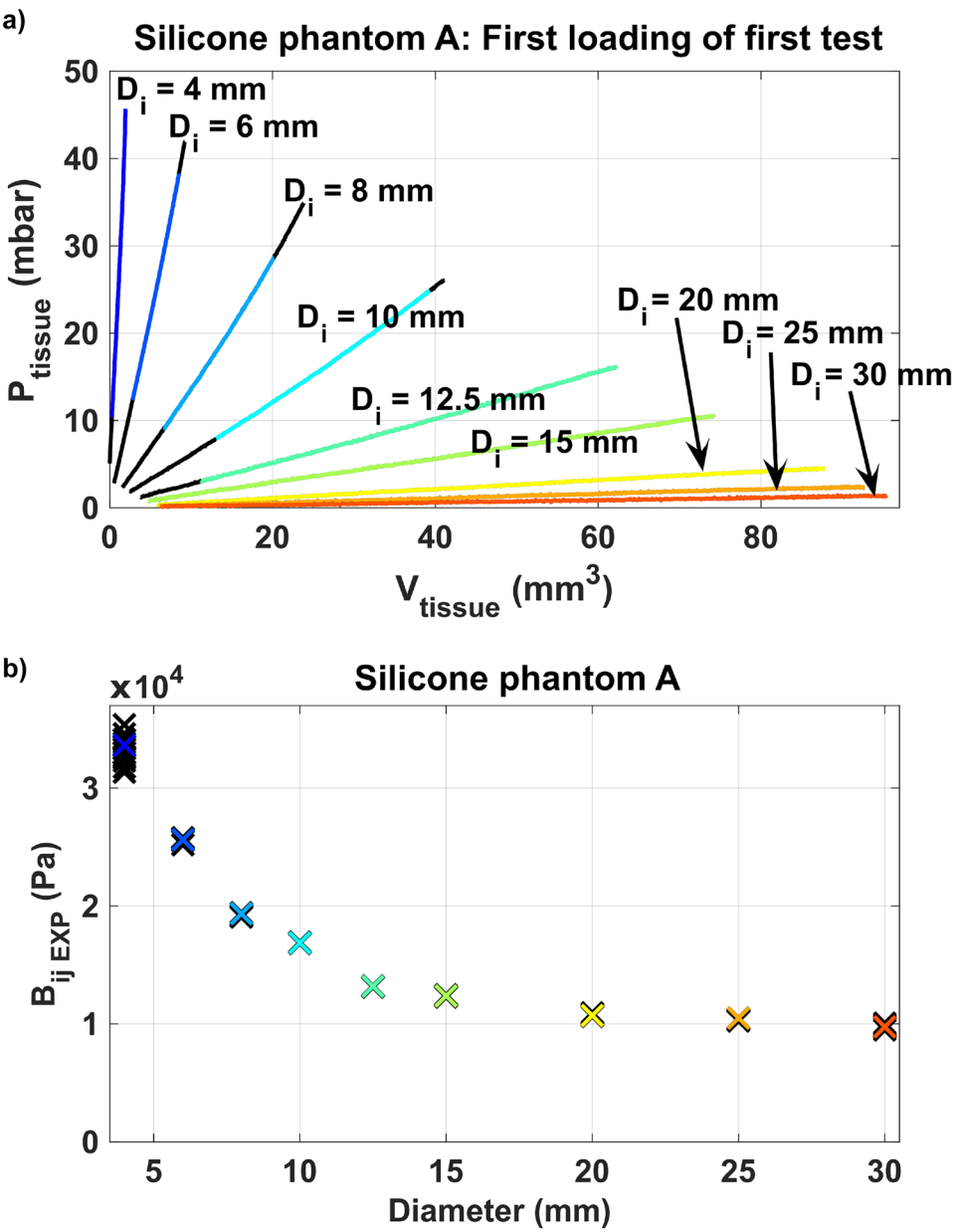

Fig. 6 **Subplot** (**a**) Example of tissue pressure-volume curves ($\Delta P_{tissue\,test} - \Delta V_{tissue\,i}$) obtained on phantom A for each aperture diameter D_i. Curve parts in colour were selected to evaluate the $B_{ij\,EXP}$ derivatives with a polynomial of degree 1. The selected parts of the curve correspond to the shape range the closest possible to $S \in [0.05, 0.15]$. **Subplot** (**b**) Bilayer material apparent stiffness B_{ij} versus aperture diameter D_i extracted for phantom A. The value $B_{ij\,EXP}$ presented in colour corresponds to the tissue pressure-volume curves ($\Delta P_{tissue\,test} - \Delta V_{tissue\,i}$) in Fig. 6(a)

Second, compared to silicone phantoms *A* (Young's moduli of 74 and 9 kPa, ratio of $\eta = 8.3$), the abdomen tissue is softer, which is in accordance with palpation. It should also be noted that the total thickness of the dermis, epidermis, and fat is approximately of 24 to 29 mm in this case (Fig. 5(b) and Table 2). The maximum aperture diameter being of $D_i = 30$ mm, the lower layer mechanical properties identification (4.8 kPa) shall be slightly affected by the mechanical properties of the muscle located under the fat. The amount of this impact has not been evaluated in this work, but it can be related to sensitivity evaluations reported in previous publications [12, 36, 40] where such influence was neglected. Other sensitivity studies can be found in the literature, such as on contact force [28], for example.

Third, the thickness of the upper layer (dermis + epidermis) was evaluated *in vivo* on the abdominal tissue. It was found to be of 2.21 ± 0.033 mm using Bmode ultrasound imaging (natural contrast between the epidermis and fat, Fig. 5(a)). Additionally, the best bilayer model that explains the experimental suction data has an upper layer thickness of 2.15 ± 0.05 mm (Table 5). The agreement between both methods (difference lower than 3%) provides a double validation: on the one hand, it shows that the layer thickness identified with the Bmode ultrasound approximately behaves as a single homogeneous upper layer during suction experiments. On the other hand, it indicates that a bilayer model is well adapted to describe suction on the skin of the abdomen with an suction diameter range from

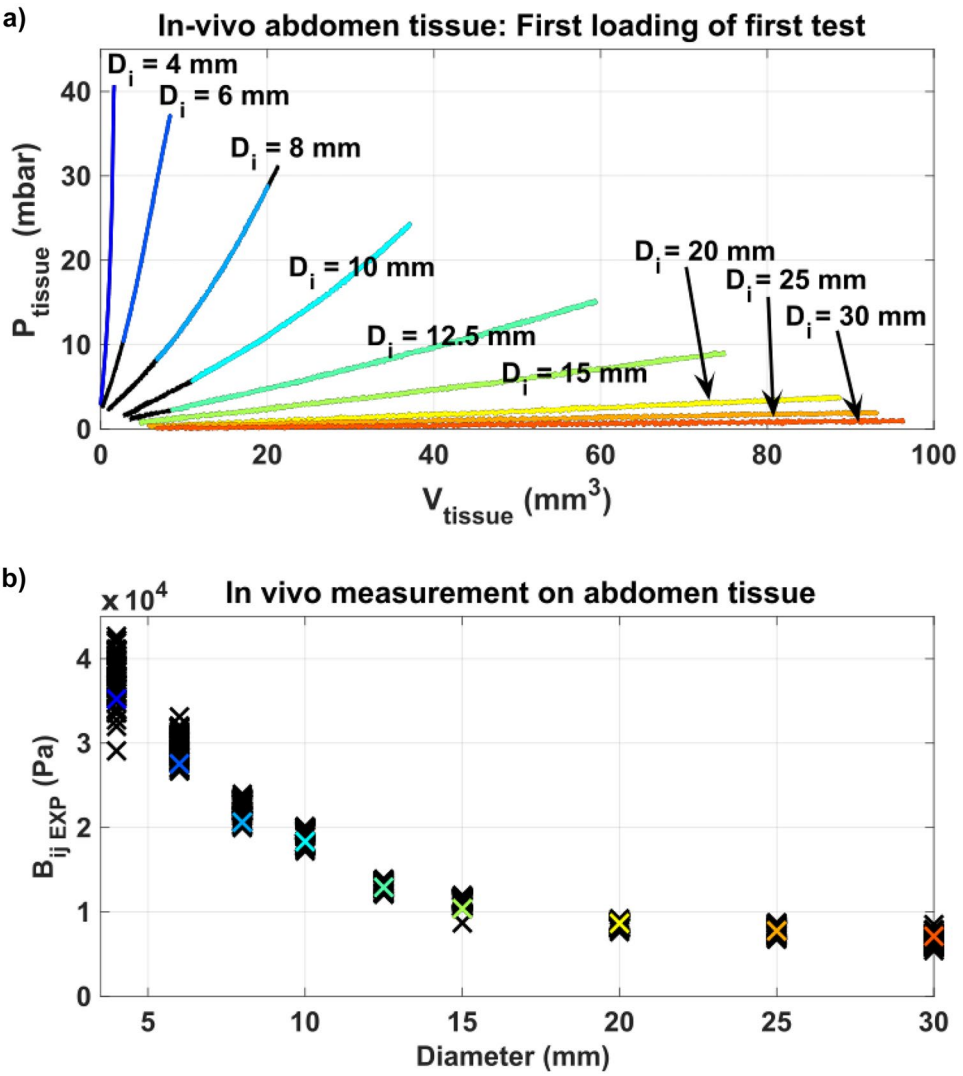

Fig. 7 **Subplot** (**a**) Example of tissue pressure-volume curves ($\Delta P_{tissue\,test} - \Delta V_{tissue\,i}$) for each aperture diameter D_i obtained *in-vivo* on the abdomen tissue of a healthy volunteer (38 years old, body mass index of 25.4). Curve parts in colour were selected to evaluate the $B_{ij\,EXP}$ derivatives with a polynomial of degree 1. The linearity of the curves is considered acceptable in this *in-vivo* case. The selected parts of the curve correspond to the shape range the closest possible to $S \in [0.05\,0.15]$. **Subplot b)** Bilayer material apparent stiffness B_{ij} versus aperture diameter D_i extracted on the abdomen tissue. The value $B_{ij\,EXP}$ presented in colour corresponds to tissue pressure-volume curves ($\Delta P_{tissue\,test} - \Delta V_{tissue\,i}$) during the first cycle in Fig. 7(a)

4 to 30 mm. This result corroborates similar assumptions made in [40] and using ultrasound or magnetic resonance measurements of the skin thickness. This eventually also gives confidence in the Young's moduli identified simultaneously with the suction method. Furthermore, the optimal thickness of the upper layer is slightly smaller (difference of 0.06 mm) than the thickness of the total skin. This result, if confirmed, could be related to the presence of a thin and soft upper layer (neglected in this contribution) identified in [26] as the epidermis and papillary layer (of 0.130 to 0.153 mm for total thickness of 1.19 and 0.97 mm, *i.e.* 10 to 16% of the total skin layer). This very thin upper layer was about 1500 times softer than the reticular dermis [26]. More studies would be required to confirm this observation.

Fourth, the experimental variances identified with both the classical and AUE methods $\sigma^2_{i\,classic}$ and σ^2_{iAUE} are almost identical for the application *in vivo* (Fig. 11(d)). It means that almost no bias was observed during the *in vivo* measurement and that the bilayer model adequately explains the experimental data. The experimental variances σ^2_{iAUE} are smaller than 8.10^{-3}, which is indeed much smaller than 1 (equation (7)). The residual norms Φ_0 are lower than their associated threshold value of $\chi^2_{df\,95\%}$ for the $P = 2$ and $P = 3$ parameter models (Fig. 11(b)). Much more experimental data would be necessary to verify that residual norms Φ_0 statistically follow the predicted chi-square distribution.

Fifth, the proposed CIs are related but should not be confused with error bars; the CIs answer the question "Where would another result be identified (with a 95% level of confidence) if the measurement was repeated with exactly the same configuration (number of points, inter and intra reproducibility) and with the same experimental variances σ^2_{iAUE} ?". Therefore, CIs have the same meaning as standard deviations. This partly explains why the tensile reference values are not always included in the computed CIs (Fig. 12). The computed CIs are yet in good accordance with the "ill-posedness" aspect of the tested case:

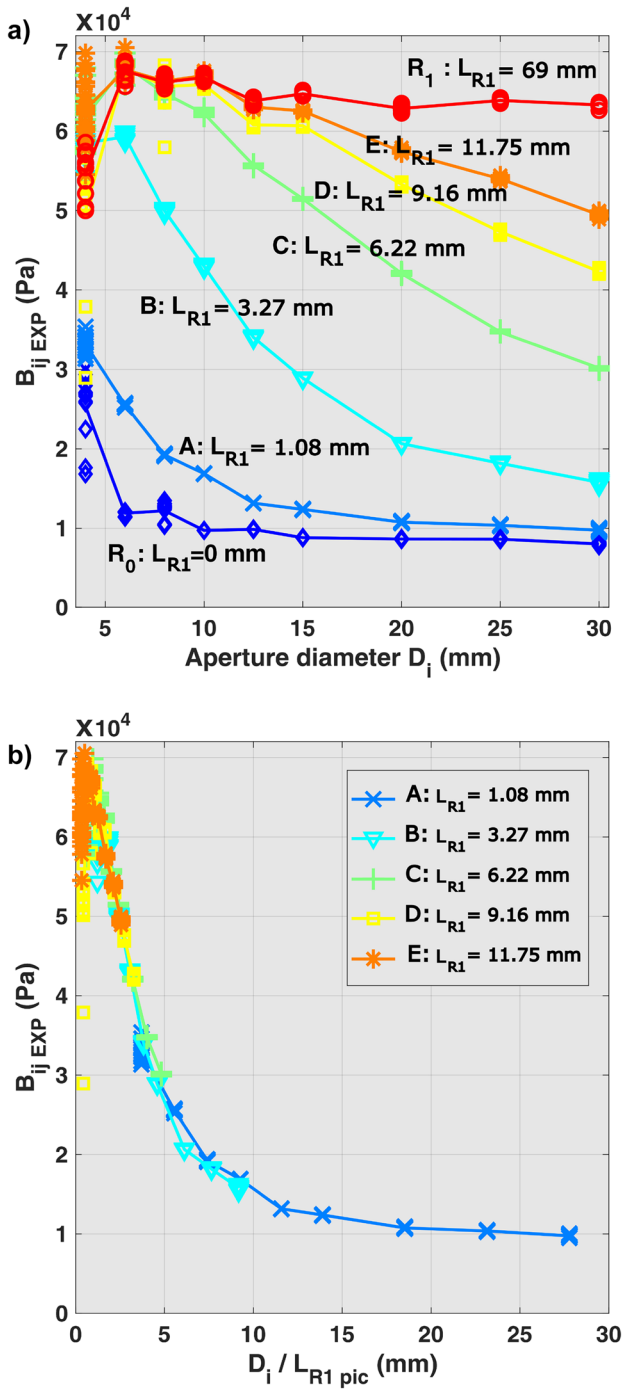

Fig. 8 Experimental results $B_{ij\,exp}$ on each bilayered and homogeneous silicone phantoms. The solid lines join the average obtained for each aperture diameter D_i. **Subplot** (**a**) Experimental results $B_{ij\,exp}$ versus aperture diameter D_i. The layer stiffness ratio $\frac{E_{R1}}{E_{R0}}$ is the same for all phantoms A to E as the same material mix was used to create all phantoms. Therefore, the experimental differences between the phantoms are due to the variation in the thickness of the upper layer L_{R1} (Table 2). **Subplot** (**b**) Experimental results $B_{ij\,exp}$ versus ratio $\frac{D_i}{L_{R1\,pic}}$ where $L_{R1\,pic}$ is evaluated during annex destructive measurements. The layer stiffness ratio $\frac{E_{R1}}{E_{R0}}$ is the same for all phantoms A to E, as highlighted by the experimental results overlap in this plot

for both $P = 2$ and $P = 3$ parameters models (Fig. 12) the Young's moduli CI of the stiff silicone R_1 decrease as the layer thickness increases. This accounts for a better identifiability of the upper layer when all the suction diameters are of the same order of size than the upper layer thickness, which is in accordance with [12]. The opposite is observed for the lower softer silicone R_0: CIs increase with the thickness of the upper layer. The mechanical behaviour of the upper layer increasingly shields the extraction of the mechanical properties of the lower layer. To the authors' knowledge, previous works only propose to compute CIs using repeatability [12, 40], comparing different measurement sites, or between subjects [25, 28]; this is the first time that real-time CI evaluation has been implemented for suction method on bilayered materials. This was possible here first by estimating the experimental variance with the AUE (including possible bias effect) and second by using the real-time simulation using the FE database interpolation.

Sixth, the CIs of $P = 3$ models are greater than for $P = 2$ for both the upper and lower identified Young's moduli. From a practical point of view, knowing the thickness of the upper layer is therefore not mandatory but can improve the final results (especially if the upper layer thickness can be accurately measured). This is a direct improvement of the method proposed in [12] where it was simply proposed to decrease the suction diameter until the apparent stiffness of the bilayer material converges.

Seventh, measurements were made from small to large cups on the abdominal tissue. Due to the ultrasound gel cord, the skin was therefore inevitably and gradually moisturised by the ultrasound gel, which may have progressively decreased the Young's modulus of the upper skin layer [47, 48]. The influence of the skin's relative humidity has not been further studied in this contribution.

As testified in reviews of the literature [40, 49–51], The mechanical properties of human skin are often measured on forearm or face, more rarely on the back, thigh, calf, abdomen, and fingertips. Direct comparisons between studies are hazardous as the experimental conditions on the one hand (testing methods, *in* or *ex vivo*, applied deformation and pressure range, loading speed, measurement location, relative humidity, subject age, *etc*.) and inverse identification procedure on the other hand (constitutive model formulation, FE models and boundary conditions for inversion, definition of the layers based on histological composition, *etc*.) significantly impact the reported values. Demonstrating the method abilities on reference phantoms was mandatory.

No data has been found in the literature on *in vivo* identification in the region of the abdomen. However, the identified elastic modulus for the skin (54 ± 1 kPa) is in full agreement with the ranges reported in the literature for

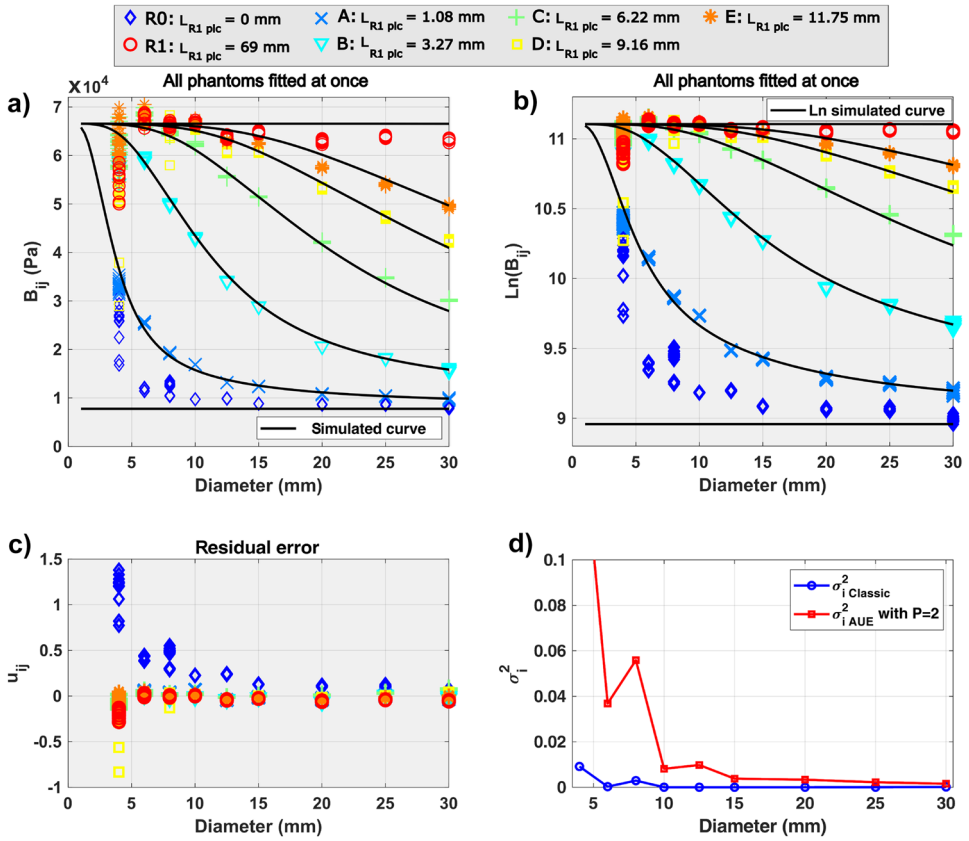

Fig. 9 Computation of a $P = 2$ parameter model over all the data on silicone phantoms to evaluate the experimental variance σ^2_{iAUE}. The results for each phantom are presented with a different colour and marker type. The optimal parameters for this fitting are $E_{R1\,all} = 83.2$ kPa and $E_{R0\,all} = 9.82$ kPa. **Subplot** (**a**) Input experimental data B_{ij} versus aperture diameter D_i. Simulated curves (in black) fitted over the data with the optimal parameters ($E_{R1\,all} = 83.2$ kPa, $E_{R0\,all} = 9.85$ kPa) and the layer thickness $L_{R1\,pic}$ of each phantom. **Subplot** (**b**) Input experimental data $Ln(B_{ij})$ versus aperture diameter D_i. Logarithm of the fitted simulated curve (in black) using the optimal parameters $E_{R1\,all} = 83.2$ kPa, $E_{R0\,all} = 9.85$ kPa and the layer thickness $L_{R1\,pic}$ of each phantom. **Subplot** (**c**) Residual error vector u_{ij} using the optimal parameters $E_{R1\,all} = 83.2$ kPa, $E_{R0\,all} = 9.85$ kPa and the layer thickness $L_{R1\,pic}$ of each phantom. **Subplot** (**d**) Identified experimental variance σ^2_{iAUE} using the residual error vector u_{ij} (equation (9)) presented in subplot (**c**). The variance $\sigma^2_{iClassic}$ computed with equation (15), Appendix B and the same set of data is also reported

human skin (0.6 to 2 160 kPa) in different locations (upper layer not including the fat) during *in-vivo* or *ex-vivo* tests (Table 6).

Some references on the mechanical properties of adipose tissue are reported in Table 7. Most identifications are obtained onto breast samples. Note that in this table, the reported Young's moduli identified using suction are qualified as "rough" or "preliminary" by the authors. The range of Young moduli for adipose tissue is from 0.12 to 29.2 kPa in the literature, the usual results being of few kPa. The elastic modulus for the fat identified in this contribution (4.8 ± 0.1 kPa) is in perfect agreement with this range.

This study comes with some limitations with respect to the proposed hardware design, the experimental protocol, and the identification method. These limitations are discussed in the following and call for future work.

Regarding hardware, the main limitation is that the same volume $\Delta V_{syringe}$ is cyclically withdrawn from the 'tissue circuit' for all aperture diameters D_i. This volume cannot be easily modified during a measurement session. The chosen volume of 0.1 mL in this study implied that the *in-vivo* pressure-shape curves (Fig. 7(a)) showed almost no non-linear behaviour for shapes smaller than 0.1. However, it would be advisable for future studies to be able to adjust the withdrawn volume $\Delta V_{syringe}$ depending on the used suction diameter. This feature would enable to observe and, hopefully, to identify the stiffening parameters of the tested tissues.

Regarding the protocol, the suction cup should be used on a flat surface and held in place with the lowest possible initial load. In any other case, the tissue sample will initially be curvaceous in the suction chamber, as also mentioned and corrected in [28]. In this contribution, initially curvaceous surfaces would modify the reference air quantity in the system and the associated calibration curve; a bias would be added to the experimental result. This is probably

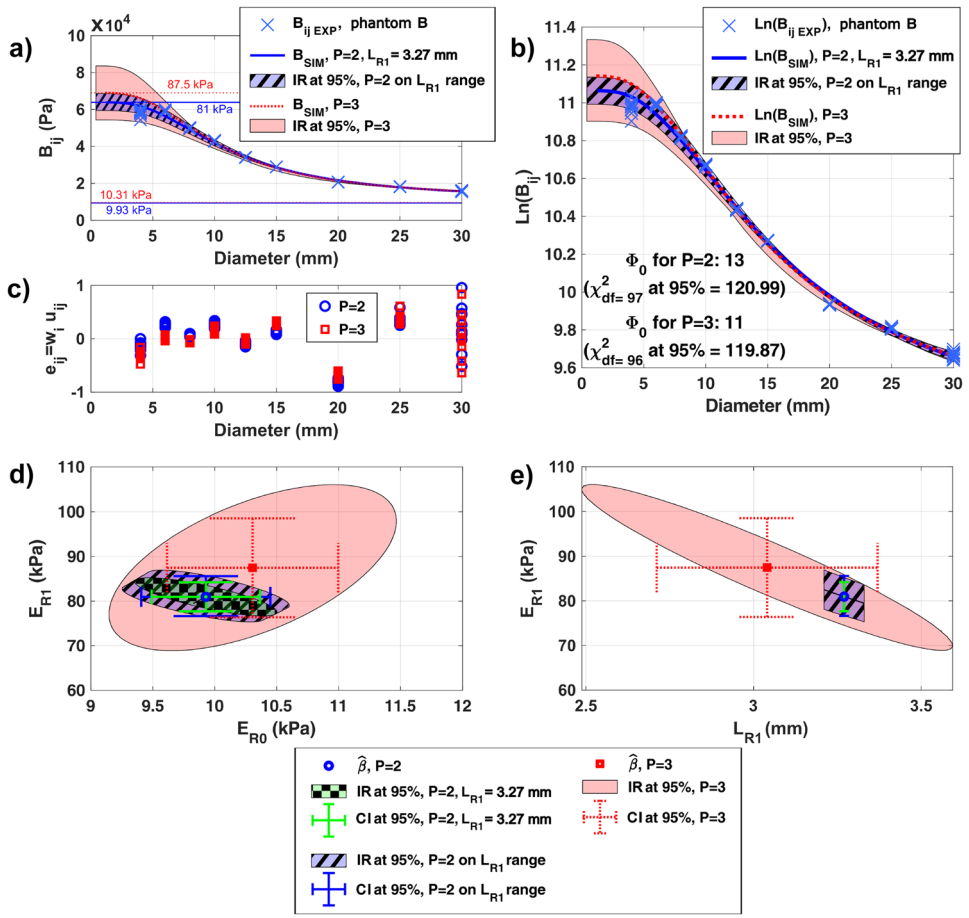

Fig. 10 Experimental data and inverse identification on experimental data of phantom *B*. **Subplot** (**a**) Experimental bilayer apparent stiffness $B_{ij\,EXP}$ for phantom B versus aperture diameter D_i. The best fitted curves are plotted along with the areas containing the curves if the parameters sweep the *P*-dimensional IR at 95% level of confidence presented in subplots (**d**) and (**e**). For homogeneous phantoms, the values of $B_{i\,SIM}$ would be independent of the aperture diameter D_i. Such cases are represented as dashed horizontal lines corresponding to the optimal identified upper and lower material Young's moduli ($E_{R1\,opt}$ and $E_{R0\,opt}$ with $P = 2$ and $P = 3$). **Subplot** (**b**) Experimental bilayer apparent stiffness $Ln(B_{ij\,EXP})$ for phantom B versus aperture diameter D_i. The best fitted curves are presented along with the areas containing the curves if the parameters sweep the *P*-dimensional IR at 95% level of confidence presented in subplots (**d**) and (**e**). The residual norm Φ_0 for $P = 2$ and $P = 3$ are both lower than the threshold at 95% of the associate chi-square law. **Subplot** (**c**) Weighted residual error vectors $e_{ij} = w_i u_{ij}$ (equation (9)) for both $P = 2$ and $P = 3$-parameters models. Note that the variances of errors e_{ij} are similar for each diameter D_i due to the use of the weighting factor $w_i^2 = 1/\sigma_{i\,AUE}^2$. The hypothesis of a disturbance with no bias (zero mean) is not perfectly met here, explaining the need to evaluate the variance with the AUE estimator. **Subplots** (**d**) The markers represent the optimal identified Young's moduli E_{R1} and E_{R0} for models with $P = 2$ and $P = 3$. The IR at 95% in the cases $P = 2$ assuming a perfectly identified layer thickness $L_{R_1\,pic} = 3.27$ mm (Table 2) is presented as a green area with a chessboard pattern. When the layer thickness sweeps its identification range $L_{R_1\,pic} = 3.27 \pm 0.05$ mm, the IR is a sum of different ellipses describing the blue area with the line pattern. The IR at 95% in the cases $P = 3$ is presented as the homogeneous red area. For each area, the corresponding CI at 95% computed with equation (14) (Appendix B) are presented with corresponding colour errorbars. Such a good overlap of the areas is not met for all phantoms and depends on the closeness between the optimal layer thickness L_{R1} and the actual layer thickness L_{R1pic}. **Subplots e)** The markers represent the optimal identified Young's moduli E_{R1} versus the layer thickness L_{R1}. The associated indifference regions are plotted in the cases $P = 2$ (assuming a layer thickness $L_{R_1\,pic} = 3.27 \pm 0.05$ mm, Table 2) and $P = 3$, respectively. The corresponding CI at 95% computed with equation (14), (Appendix B) are presented with corresponding colour errorbars

what happened during the experiments on the homogeneous soft phantom R_0 (Fig. 8)) where no stiff superficial layer stabilised the initial shape. Furthermore, surface local curvature shall affect airtightness for large aperture diameters, preventing their use. Eventually, performing measurements *in vivo* shall provide data with more noise (breathing, muscle activation, *etc.*) averaged over the cycles. The impact of these phenomena on the entire identification process should be better evaluated in future studies.

In this work, the developed experimental *in-vivo* process took about 15 minutes for each aperture diameter (including setting, thermal stabilisation, repeatability measurement,

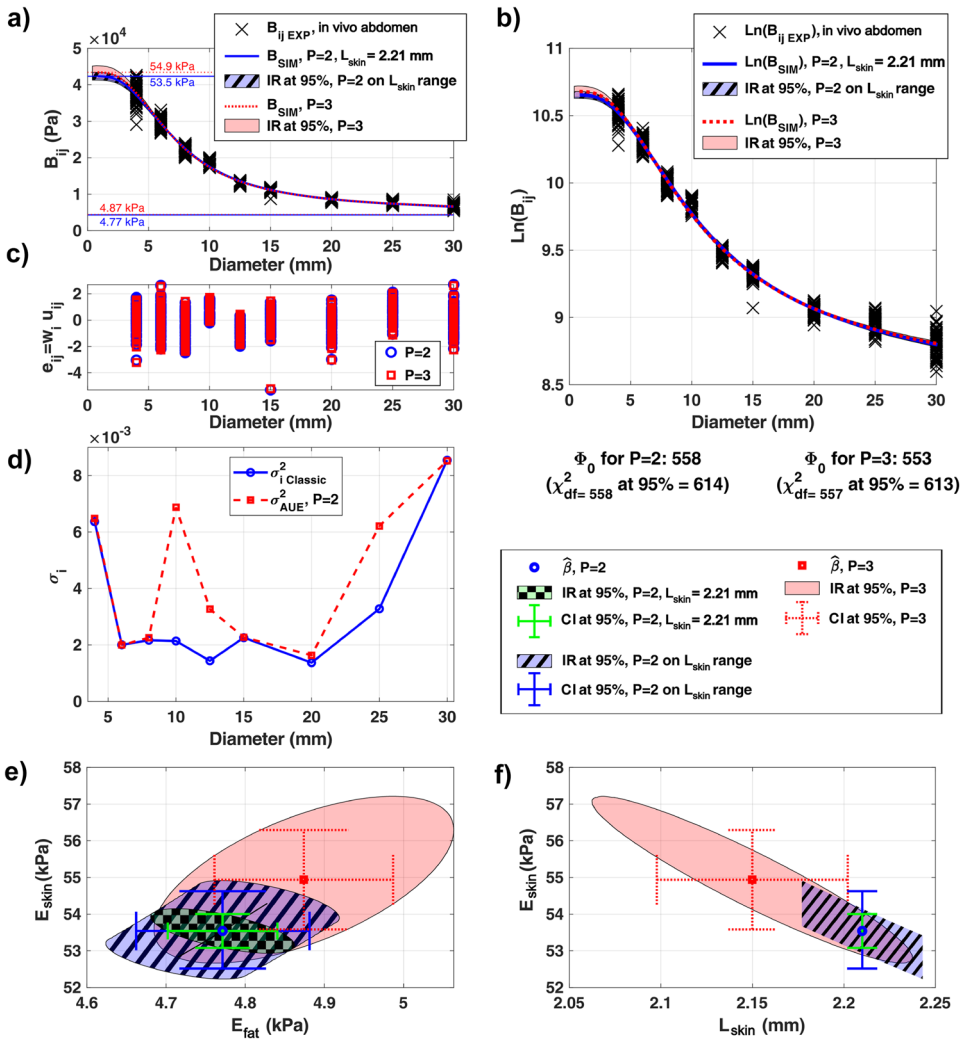

Fig. 11 *In-vivo* experimental data and inverse identification on the abdomen tissue of a healthy volunteer. **Subplot** (**a**) Experimental bilayer apparent stiffness $B_{ij\,EXP}$ in the abdomen versus aperture diameter D_i. The best fitted curves are plotted along with the areas containing the curves if the parameters sweep the P-dimensional IR at 95% level of confidence presented in subplots e) and f). **Subplot** (**b**) Experimental bilayer apparent stiffness $Ln(B_{ij\,EXP})$ on the abdomen versus aperture diameter D_i. The best fitted curves are presented along with the areas containing the curves if parameters sweep the P-dimensional IR at 95% level of confidence presented in subplots e) and f). The residual norm Φ_0 for $P = 2$ and $P = 3$ are both lower than the threshold at 95% of the associate chi-square law. **Subplot** (**c**) Weighted residual error vectors $e_{ij} = w_i u_{ij}$ (equation (9)) for both $P = 2$ and $P = 3$-parameters models. Note that the variances of errors e_{ij} are similar for each diameter D_i due to the use of the weighting factor $w_i^2 = 1/\sigma_{i\,AUE}^2$. **Subplots** (**d**) Identified experimental variance $\sigma_{i\,AUE}^2$ using the residual error vector u_{ij} (equation (16), Appendix B). The variance $\sigma_{i\,Classic}^2$ calculated with equation (15) (Appendix B) is also reported. The hypothesis of a disturbance with no bias (zero mean) is not perfectly met here as both variances are not perfectly overlapping. **Subplots** (**e**) The markers represent the optimal identified Young's moduli E_{skin} and E_{fat} for models with $P = 2$ and $P = 3$. The IR at 95% in the cases $P = 2$ assuming a perfectly identified layer thickness $L_{skin\,US} = 2.21$ mm (Table 2) is presented as a green area with a chessboard pattern. When the layer thickness sweeps its identification range $L_{skin\,US} = 2.21 \pm 0.033$ mm, the IR is a sum of different ellipses describing the blue area with the line pattern. The IR at 95% in the cases $P = 3$ is presented as the homogeneous red area. For each area, the corresponding CI at 95% computed with equation (14) (Appendix B) are presented with corresponding colour errorbars. **Subplots** (**f**) The markers represent the optimal identified Young's moduli E_{skin} versus layer thickness L_{skin}. The associated indifference regions are plotted in the cases $P = 2$ (assuming a layer thickness $L_{skin\,US} = 2.21 \pm 0.033$ mm, Table 2) and $P = 3$, respectively. The corresponding CI at 95% computed with equation (14) (Appendix B) are presented with corresponding color error bars

and removal). The whole experimental process, including 9 different cups, is obviously still too time-consuming for direct routine clinical application. Therefore, the experimental protocol will need further simplification, for example, by reducing the number of required suction diameters, reproducibility cycles, *etc*. These points will be evaluated during further work so as not to compromise the performance of the method.

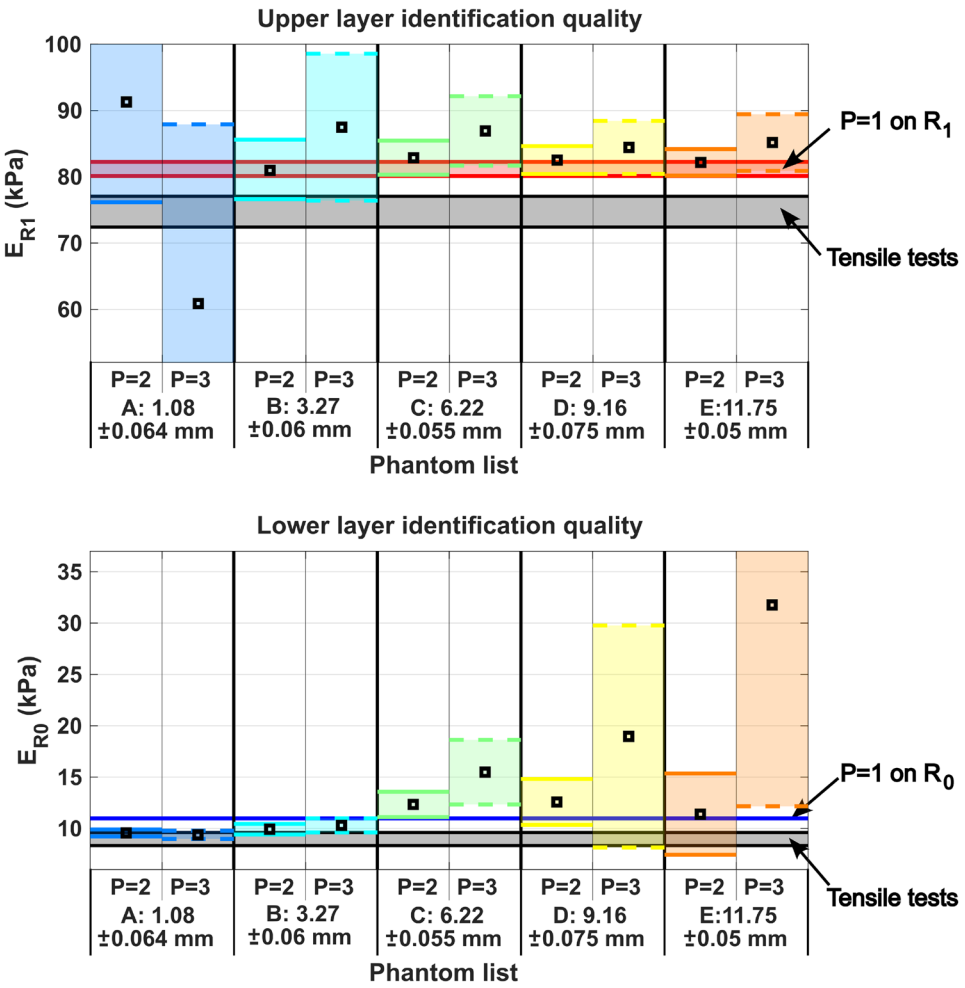

Fig. 12 Experimental indifference ranges on phantoms *A* to *E*. **Subplot** (**a**) Identification ranges for the upper layer R_1 using a $P = 2$ or $P = 3$-parameters model. The horizontal black band represents the region of indifference of the tensile test at 95% (average ± 2 Std) on silicone R_1. The horizontal red band represents the 95% indifference region on suction using a $P = 1$-parameter model on the homogeneous phantom R_1. **Subplot** (**b**) Identification ranges for the lower layer R_0 using a $P = 2$ or $P = 3$-parameters model. The horizontal black band represents the tensile test indifference region at 95% (average ± 2 Std) on silicone R_0. The horizontal blue band represents the 95% indifference region on suction using a $P = 1$ -parameter model on homogeneous phantoms R_0

Regarding the inverse analysis procedure, the thickness of the bilayer tissue is considered to be higher than the biggest aperture diameter ($D_i = 30$ mm in this contribution). Such a configuration should be satisfied experimentally, which will naturally be the case, for example, for breast or abdominal tissue. For tissues of smaller thickness, the protocol can be applied excluding the larger suction diameters. In future work, the FE database will also be adapted to accommodate other bottom boundary conditions to account for the mechanical influence of muscle or bone beneath the bilayer tissue.

The quality of CI evaluation directly depends on the correct identification of the experimental variances σ^2_{iAUE} (equation (16), Appendix B). Unfortunately, their identification is very sensitive to bias and usually requires the acquisition of many data (repeatability). This requirement could be difficult to achieve during clinical applications. Using the AUE tool partly fixes this difficulty, but more work should be done to evaluate typical experimental variances depending on the location on the body (breathing, muscle activation, *etc*.).

Conclusion

A new suction system has been developed. It is based on the application of a partial cyclic vacuum to the tested tissue to evaluate its apparent mechanical properties at moderate tissue strain. The system suction head can be easily switched for aperture diameters D_i between 4 and 30 mm. The developed identification method enables, almost in real-time, to identify mechanical Young's moduli and the upper layer thickness of bilayered structures interpolating an off-line finite element database. Confidence intervals inferred from the minimized cost function are also provided.

The system was tested on controlled bilayer phantoms for upper layer thickness from 1 to 12 mm. The bilayer phantom with an upper layer of 3 mm presented the best parameter identifiability for both Young's moduli (relative errors lower than 10% compared to reference values obtained during tensile tests). The upper layer thickness was also identified with an error lower than 2%. For other upper layer thickness, identified results were of the proper order of magnitude. The

obtained indifferences regions in each case were representative of the identification quality and "ill-posedness" of the experimental situation.

The method has been applied successfully *in vivo* to the abdominal tissue of a healthy volunteer. The thickness of the upper layer (dermis + epidermis) was evaluated to be 2.21 mm using Bmode ultrasound imaging and 2.15 ± 0.05 mm with the suction method. The identified Young's modulus was 54 kPa on the skin (dermis and epidermis) and 4.8 kPa on the underneath fat. These preliminary results are in good agreement with the literature and give confidence for future applications.

In future work, the authors intend to apply the VLASTIC method to estimate the mechanical properties of the most accessible soft tissues, such as, for example, skin and fat stiffness for breast [52], abdomen, face [53, 54], sacrum [55] or foot [56].

Appendix A: Real time Evaluation of the Simulated Apparent Stiffness

The apparent stiffness $B_{i\,SIM}(\beta,\theta)$ is the slope of the pressure-shape curve at shape $S = 0.1$ (equation (6), main paper body) when aspirating a bilayer phantom. This simulated stiffness is evaluated many times to find iteratively the minimum of the cost function Φ_{Param} (equation (8), main paper body) or to evaluate the identifiability of the material parameters (Appendix B). The apparent stiffness $B_{i\,SIM}(\beta,\theta)$ depends mainly on the different combination of four parameters, which are the aperture diameter D_i, the upper layer Young's modulus E_{R1} and its thickness L_{R1}, and the lower layer Young's modulus E_{R0} (Fig. 3).

If the simulated apparent stiffness $B_{i\,SIM}(\beta,\theta)$ was evaluated using, for example, a FE model implemented and updated for each calculation point, the time required to solve a single inverse identification would be phenomenal. Therefore, this appendix describes how the simulated apparent stiffness $B_{i\,SIM}(\beta,\theta)$ was evaluated in real time. The idea is mainly to define and interpolate precalculated abacuses as discussed in [57].

Four main steps are required:

1. Reducing, if possible, the number of parameters required for the database ("Database Definition"),
2. Defining a FE model for the suction experiment and creating the database in the required parameter range ("FE Model"),
3. Interpolate the database for any parameters D_i, L_{R_1}, E_{R1} and E_{R0} ("Database Interpolation"),
4. Validate the proposed method ("Validation").

A.1 Database definition

The four main parameters D_i, L_{R_1}, E_{R1} and E_{R0} can be combined to reduce the required dimension of the FE database from 4 to 2.

Scale Effect : assuming the lower layer thickness is infinite (in practice, the total thickness of the layer is much larger than the aperture diameter D_i), the upper layer relative contribution to the shape S_{tissue} is governed only by the depth ratio $\zeta = \frac{D_i}{L_{R_1}}$ between the aperture diameter D_i and upper layer thickness L_{R_1} [12]; redundant depth ratio ζ provides redundant information in the FE database.

Material Stiffness Contrast : considering a material stiffness contrast ratio $\eta = \frac{E_{R1}}{E_{R0}}$, the apparent stiffness $B_{i\,SIM}(\beta,\theta)$ can be seen as proportional to the bottom layer stiffness E_{R0} (equation (10)).

The required FE database to compute the apparent stiffness $B_{i\,SIM}(\beta,\theta)$ can thus be reduced to evaluate a two-parameter function, f_{sim}, so that:

$$B_{i\,SIM}(\beta,\theta) = E_{R0} f_{sim}(\zeta,\eta) \tag{10}$$

where f_{sim} is an adimensional function depending on the depth ratio $\zeta = \frac{D_i}{L_{R_1}}$ and on the layer stiffness contrast ratio $\eta = \frac{E_{R1}}{E_{R0}}$.

Note that equation (10) implies that the cost function Φ_{Param} (equation (8), main paper body) is linearly conditional on the parameter E_{R0} [44]. It means that once ζ and η are chosen, the parameter E_{R0} minimising Φ_{Param} is simply obtained by solving a linear problem.

The range of both the ratio parameters ζ and η were chosen to build the database, *i.e.* to estimate the function $f_{sim}(\zeta,\eta)$:

1. The chosen range for the stiffness contrast ratio η was from 1 to 120 to anticipate application to *in-vivo* cases.
2. Aspirating with an aperture of diameter D_i extracts data mainly at a depth of one diameter [12]. Let us consider the case where the layer thickness is greater than D_i, *i.e.* for example, $L_{R_1} > 3D_i$. A small increase of the layer thickness should have negligible influence on the result in this case [12, 36, 40]. Therefore, a limit scale ratio $\zeta = \frac{D_i}{L_{R_1}} > \frac{1}{3}$ was chosen. Moreover, the smallest aperture diameter being of $D_i = 4$ mm, it was decided that the identification of mechanical properties of layers thinner than 0.25 mm would be out of the identification range of this work. The largest aperture diameter being of $D_i = 30$ mm, the maximum depth ratio ζ for such a thin layer is of 120. Therefore, the range of the scale ratio ζ required in this work was $[\frac{1}{3}, 120]$.

Table 8 Comparison between the apparent stiffness computed by interpolating the PCA analysis ($B_{i\,SIM\,PCA}$) or with a FE model ($B_{i\,SIM\,FE}$) implementing the exact parameters D_i, L_{R_1}, E_{R1} and E_{R0}. The data input and output for the FE models are highlighted in light grey. The data input and output for the *PCA* estimation are highlighted in darker grey (equation (12)). For illustration, the particular interpolated points for $f_{sim\,PCA}$ are plotted in (Fig. 15) using the markers reported in first column

	D_i (mm)	L_{R_1} (mm)	$\zeta = \frac{D_i}{L_{R_1}}$	E_{R0} (kPa)	E_{R1} (kPa)	$\eta = \frac{E_{R1}}{E_{R0}}$	$f_{sim\,PCA}$ (No unity)	$B_{i\,SIM\,PCA}$ (kPa)	$B_{i\,SIM\,FE}$ (kPa)	RE (%)
▷	4	8	0.5	14	49	3.5	2.74	38.628	38.367	0.68
□	6	6	1	10	135	13.5	10.4	104.89	103.99	0.87
▽	8	3.47	2.3	12	282	23.5	13.82	166.92	165.92	0.60
◊	10	3.23	3.1	9	301.5	33.5	14.48	130.84	130.36	0.37
◁	12.5	2.78	4.5	11	478.5	43.5	10.60	117.68	116.61	0.92
☆	20	2.94	6.8	13	695.5	53.5	6.31	82.785	82.090	0.85
△	25	2.17	11.5	5	317.5	63.5	3.22	16.266	16.110	0.97

FE Model

Model Definition

An FE model was parameterized using a Matlab code to provide $f_{sim}(\zeta, \eta)$ for the chosen ranges of ζ and η:

$$f_{sim}(\zeta, \eta) = \frac{B_{i\,SIM\,db}}{E_{R0\,db}} \tag{11}$$

where $B_{i\,SIM\,db}$ is the slope of the FE pressure-shape curve. To compute the database, an arbitrarily chosen lower layer stiffness of $E_{R0\,db} = 4000$ Pa was used.

A static, implicit, axisymmetric model (ANSYS APDL) was defined to describe suction onto cylindrical phantoms. The model takes into account large displacements. A constant aperture diameter of $D_i = 10$ mm was chosen (Fig. 13(a)); the depth ratio $\zeta = \frac{D_i}{L_{R_1}}$ was changed by modifying the layer thickness L_{R_1}. To allow the use of a unique mesh for all simulations in the database, a geometry of $M = 20$ pre-meshed layers was defined (Fig. 13(b)). The ratio $\zeta = \frac{D_i}{L_{R_1}}$ was thus modified between simulations by attributing a Young modulus of $E_{R1\,db}$ to the first $[1, m]$ upper-layers and a Young's modulus of $E_{R0\,db}$ to the other layers in $[m+1, M]$. The mesh used to compute the whole database was composed of 6 bilinear axisymmetrical elements ($Q8$, Plane183, ANSYS) in each layer thickness. A zoom-in of the mesh size is reported in Fig. 13(b).

Note that the parts of the 3D printed cups in contact with the tissue (wall thickness, fillet radius) were all proportional to the cup aperture D_i; the model cup geometry in contact with the phantom is representative of the reality for all cup sizes.

The boundary conditions are presented in Fig. 13(a). The vertical line AG is the axisymetric axis of the model; a single planar section of the model defines the whole model geometry. The top of the suction aperture (line CD) is clamped in all directions. A partial vacuum $-\Delta P_{tissue}$ is applied to the line AB. Contact elements were defined between the suction aperture and the line AB. With these boundary conditions, the whole tissue is free to move up or down relatively to the cup, depending on the applied pressure $-\Delta P_{tissue}$. These boundary conditions account for the fact that external loads applied on the cup were as small as possible during the experiments (Fig. 4, illustration on phantom A). No additional external loads were taken into account in the simulations. Furthermore, the dimensions of the phantom were large enough so that the application of a rigid casing outside the tissue phantom (Fig. 13(a)) had a negligible impact on the aspirated volume (numerically tested).

The material of aperture and, optionally of the rigid casing, were modelled with an elastic Hookean model with steel mechanical properties. An incompressible Neo-Hookean model simulated the material behaviour of each tissue layer. The apparent stiffness $B_{i\,SIM\,db}$ was evaluated at shapes equal to 0.1; for such a small deformation state, the incompressibility of the material (Poisson coefficient $\nu \in [0.45\ 0.5[$) did not influence the results (numerically tested).

The friction coefficient between the tissue and the cup was chosen of $f = 0.2$. During the experiment, this parameter was actually unknown and was affected by the ultrasound gel cord. The influence of the friction coefficient has been tested numerically (no friction to glued boundary conditions). Its effect was considered negligible (as also reported in [58]) when the upper layer is stiffer than the lower layer.

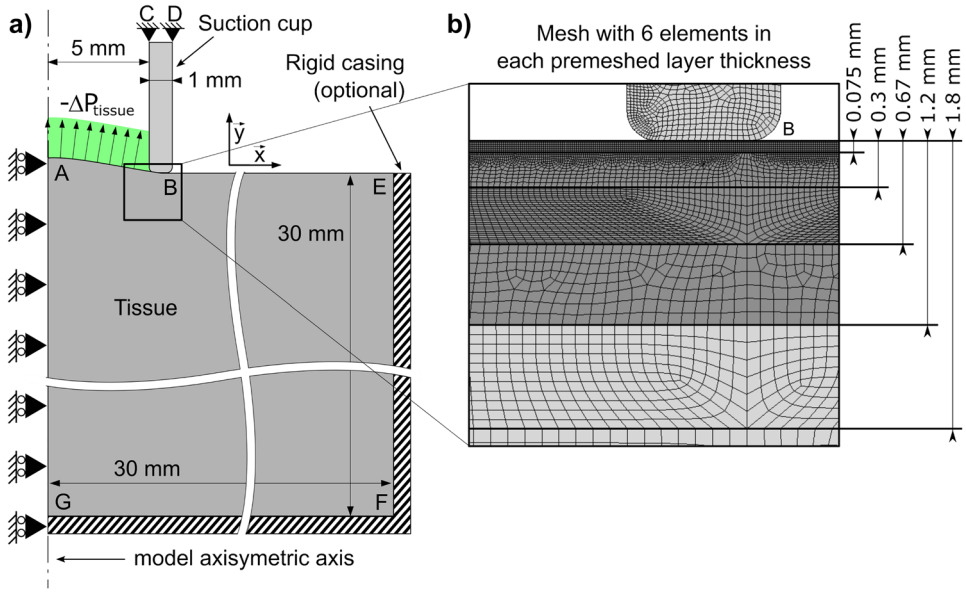

Fig. 13 Axisymmetric FE model. **Subplot** (**a**) Geometry, boundary conditions, and main dimensions. The nodes of the CD line are completely clamped. Line AG nodes cannot move horizontally and are free in the vertical direction to account for the axisymmetric conditions. A partial vacuum homogeneous pressure $-\Delta P_{tissue}$ is applied to the AB line and is represented by the green area and arrows. Contact elements are defined between the line AB and the suction aperture. Note that with the defined boundaries conditions, the suction cup is fixed and the tissue can freely move up and down into the suction aperture under partial vacuum $-\Delta P_{tissue}$. This set of boundary conditions ensures that load between tissue and suction aperture is only due to the cup internal pressure; no external normal or shear loads are added to the model. **Subplot** (**b**) Local mesh zoom in: pre-meshed layers are defined at different depths ($L_{R_1} = \{0.075, 0.3, 0.67, 1.2, 1.8, ...\}$) to use the same converged mesh for all calculations in the database (six Q8 element minimum in each layer thickness, noted Mesh 6). The mechanical property of the material E_1 is applied to the elements of the upper pre-meshed layers (illustration of the layer thickness $L_{R_1} = 1.2$ presented as a darker gray, *i.e.* a ratio $\zeta = 8.3, m = 4$)

The model solution was computed for an initial small partial vacuum $-\Delta P_{tissue}$. The 2D displacement of line AB was converted by numerical integration into the simulated volume V_{tissue} aspirated into the cup. This volume was normalised into shape S_{tissue} (equation (4)), main paper body). The partial vacuum $-\Delta P_{tissue}$ was gradually and monotonically increased. The output result needed to include the shape $S_{tissue} = 0.1$ to be validated (Fig. 14(a)). The results obtained around this reference shape were used to compute the sought slope $B_{i\,SIMdb}$, which provided in turn the adimensional value f_{sim} (equation (11), illustration in Fig. 14(b)) for $\eta = \frac{E_{R1}}{E_{R0}} = 120$).

The FE database was calculated on stiffness ratios ranges: $\eta = \frac{E_{R1}}{E_{R0}} \in [1,\ 120]$ and $\zeta = \frac{D_i}{L_{R_1}} \in [\frac{1}{3},\ 133]$ (Fig. 15).

Mesh Convergence

To be trustworthy, the database results should be independent of the mesh used. To test this point, a specific curve of the simulation output f_{sim} is presented for 6 meshes with different sizes. Mesh 1 is the coarsest mesh, with only 1 elements in each pre-meshed layer thickness (6 561 elements in the tissue). The number of elements in each pre-meshed layer thickness is progressively increased up to 6 elements (65 918 elements in the tissue). The thinnest mesh is noted Mesh 6 (Fig. 13(b)).

The case with the stiffness contrast ratio $\eta = \frac{E_{R1}}{E_{R0}} = 120$ was considered to be the most demanding case, *i.e.* inducing stress concentrations that could most affect the results. The curve of interest f_{sim} is presented in (Fig. 14(b)) for all 6 meshes. At first sight, all the results overlap. A closer inspection (zoom-in Fig. 14(b)) confirms that the curves obtained for all 6 meshes are slightly different. The convergence of this curve is illustrated in Fig. 14(c) for different depth ratios $\zeta = \frac{D_i}{L_{R_1}}$ and taking the output curve of Mesh 6 as reference to compute relative variations. Therefore, the variations between Mesh 1 and 6 are less than 2% even if the total number of elements is multiplied by 10. Mesh 6 is considered converged and has been used to compute the entire database.

Database Interpolation

The database (Fig. 15) was analysed using the Principal Component Analysis (PCA) method (based on the well

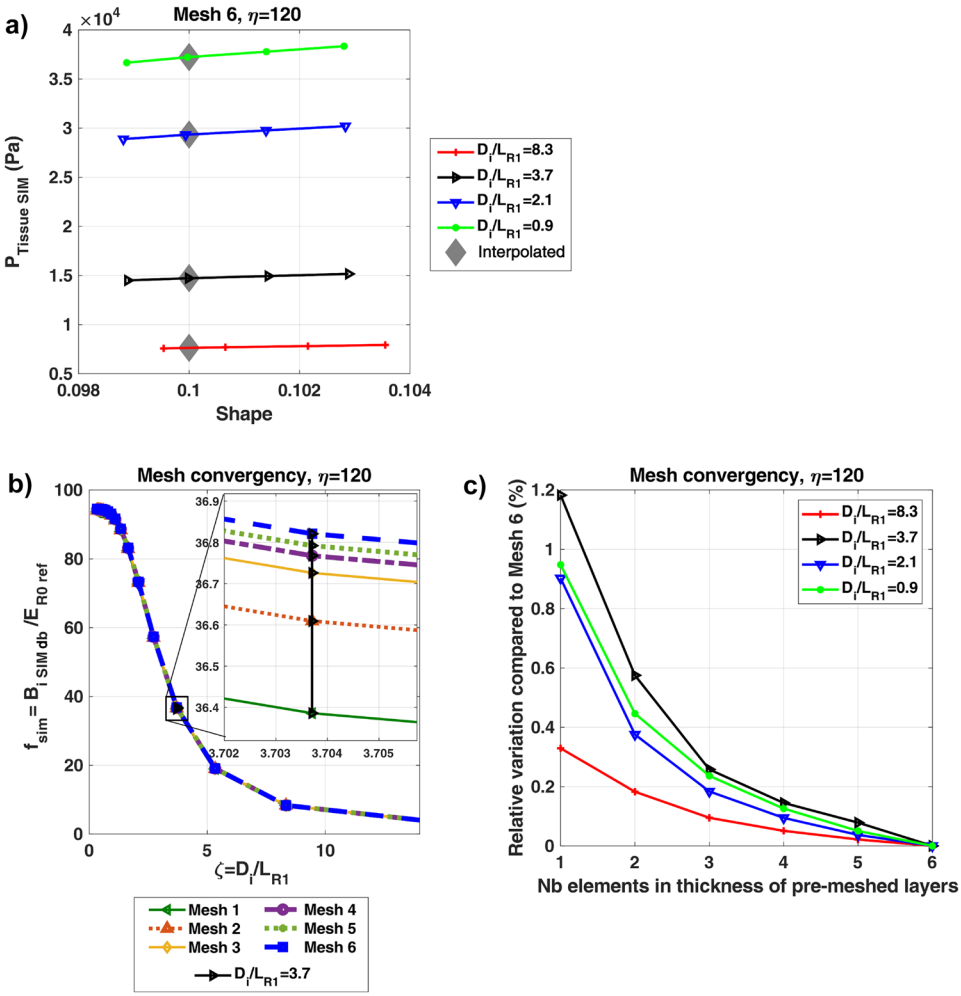

Fig. 14 Mesh convergence demonstration for a specific database curve f_{sim}. **Subplot** (**a**) Pressure-shape curves obtained for the thinnest mesh (Mesh 6), for a stiffness ratio $\eta = \frac{E_{R1}}{E_{R0}} = 120$ and different values of the depth ratio $\zeta = \frac{D_i}{L_{R_1}}$. **Subplot** (**b**) Simulation output curve f_{sim} for a stiffness ratio $\eta = \frac{E_{R1}}{E_{R0}} = 120$. The output curves for 6 different meshes (from coarse to thin) overlap in this plot. Local zoom-in for a depth ratio $\zeta = \frac{D_i}{L_{R_1}} = 3.7$ illustrates convergence with mesh refinement. **Subplot** (**c**) Relative variations of f_{sim} for meshes 1 to 6 (total number of elements in the model multiplied by 10) using the results of Mesh 6 as reference

known Singular Value Decomposition method). For a detailed description of the model reduction using the PCA method, the reader is kindly referred to [59]. Only the 3 first eigenvectors and associated weighting functions were kept, representing more than 99.99% of the database information:

$$f_{sim\,PCA}(\zeta,\eta) = f_{sim0} + \sum_{p=1}^{3} \alpha_p(\eta)\ V_p(\zeta) \tag{12}$$

where $V_p(\zeta)$ are the three first PCA normalised eigen vectors and $\alpha_p(\eta)$ are the associated weighing functions. $f_{sim0} = 0.7885$ is the FE output for a stiffness ratio $\eta = 1$ subtracted from the database prior to PCA. The eigen vectors $V_p(\zeta)$ and their spline interpolation are presented in Fig. 16(a). The weighing functions $\alpha_p(\eta)$ are presented in Fig. 16(b) and (c). Note that the database is dominated by the first weighing function $\alpha_1(\eta)$ and associated first eigen vector $V_1(\zeta)$; the simulated value $f_{sim\,PCA}$ is mainly proportional to the first eigen vector $V_1(\zeta)$.

Database interpolation results using the PCA is presented as black continuous curves in Fig. 15. Although each point of Fig. 15 required to solve a FE model for different partial vacuums $-\Delta P_{tissue}$, the interpolation of the whole database requires only the interpolation of the eigen vectors and weighing function in equation (12). Also note that any other interpolation scheme could have been chosen to interpolate the FE database.

Validation

To validate the apparent stiffness $B_{i\,SIM}(\beta,\theta)$ predicted by the PCA interpolation (equations (12) and (10)), additional tests were performed. Seven FE models were created with overmeshed models (200 elements in diameter D_i) and implementing the exact parameters D_i, L_{R_1}, E_{R1} and E_{R0}. The other parameters of the model were kept similar to the ones used to compute the whole database.

The input parameters and the associated apparent stiffness results by direct FE simulation or PCA interpolation ($B_{i\,SIM\,FE}$ and $B_{i\,SIM\,PCA}$, respectively) are reported in Table 8. Note that both the dimension ratio ζ and the stiffness ratio η were chosen so as not to be directly represented in the database (Figs. 15 and 16). For all tests performed, the relative error between the PCA and the direct FE model is less than 1%, which is considered to be fully satisfactory.

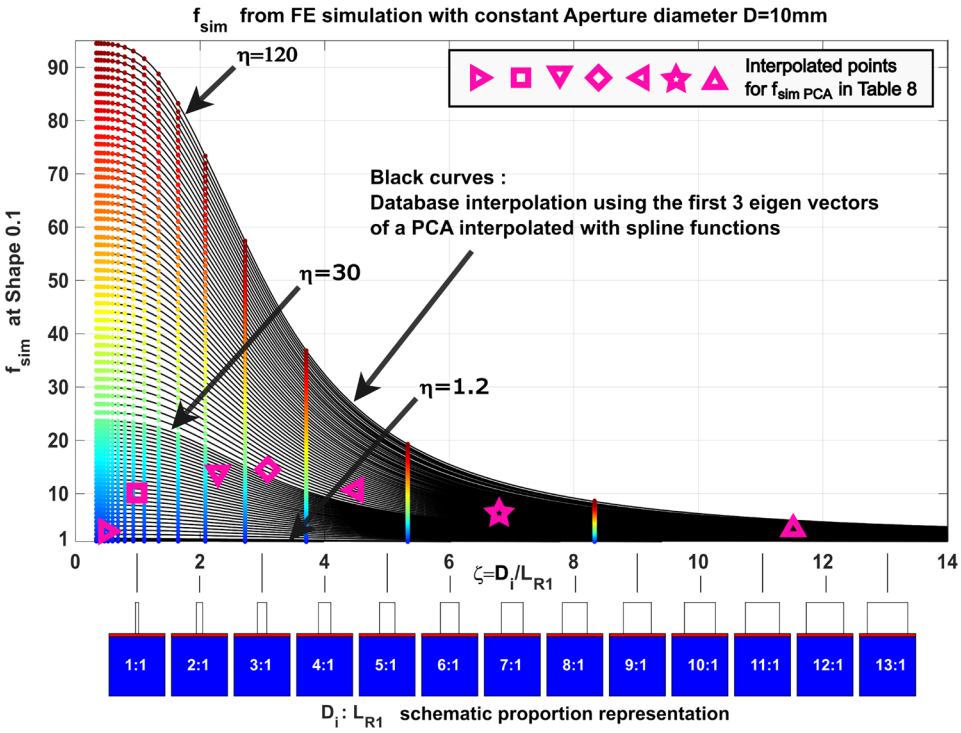

Fig. 15 The FE normalized results f_{sim} (equation (11)) in the database are represented as coloured point markers versus depth ratio $\zeta = \frac{D_i}{L_{R_1}}$. The stiffness ratios range is $\eta = \frac{E_{R1}}{E_{R0}} \in [1, 120]$. Interpolation of the PCA eigen vectors and weighing functions enables interpolation of the database (equation (12)), as presented with the black curves joining the point markers. Integer values of depths ratio $\frac{D_i}{L_{R_1}}$ are visually represented under the abscissa axis. Illustrations of particular interpolated points $f_{sim\,PCA}$ (equation (12)) used to compute the values $B_{i\,SIM\,PCA}$ in Table 8 are also reported as specific markers. Consult Table 8 for corresponding legend

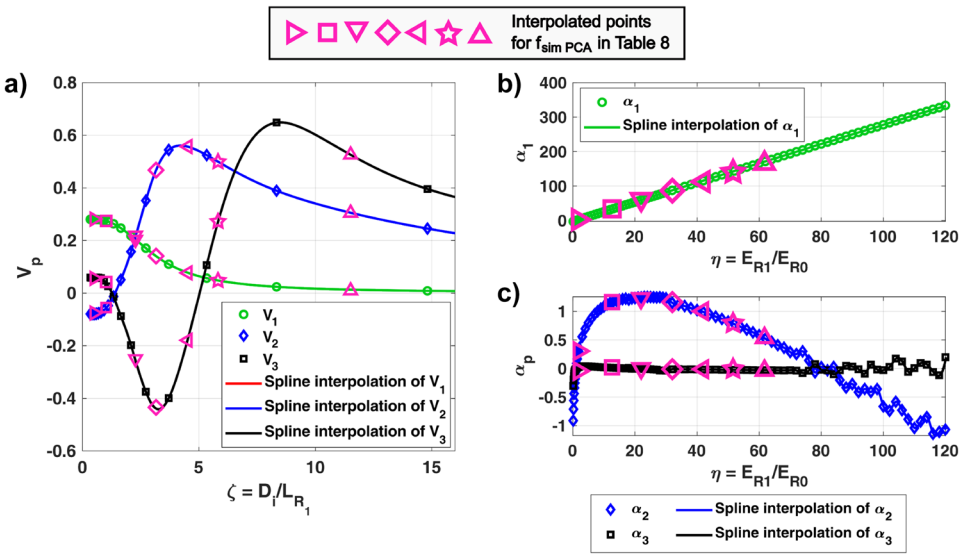

Fig. 16 PCA three first eigen vectors and weighing functions representing the FE database (equation (11)). Illustrations of particular interpolated points on the eigen and weighing functions to compute $f_{sim\,PCA}$ (equation (12)) and $B_{i\,SIM\,PCA}$ (equation (10)) in Table 8 are also reported in this figure as specific markers. Consult Table 8 for corresponding legend. **Subplot** (**a**) Three first normalised eigen vectors and associated interpolation with splines. **Subplot** (**b**) Pondering functions α_1 and spline interpolation. **Subplot** (**c**) Pondering functions α_2 and α_3 and spline interpolation

Appendix B: Parameters' Identifiability and Experimental Variance

As mentioned in the main body of the paper, choosing weights w_i^2 representative of the experimental variance σ_i^2 is important if the parameter identifiability is directly inferred from the cost function Φ_{Param} (equation (8), main paper body). This appendix develops the mathematical approach chosen to evaluate the parameter identifiability and the variance estimation derived from the residual vector u_{ij}.

Parameters' Identifiability

The parameter identifiability under heteroscedastic variance is usually computed using different variance-covariance estimators [42, 43]. In this work, a classic variance-covariance matrix $\widehat{V}_{WLS}$ is used [43]:

$$\widehat{V}_{WLS} = \left[F^T\left(\widehat{\beta}\right) F\left(\widehat{\beta}\right)\right]^{-1} \tag{13}$$

where $F\left(\widehat{\beta}\right)$ is the $N_m \times P$ Jacobian matrix of the function $w_i\, Ln\left(B_{i\,SIM}(\beta,\theta)\right)$ (equation (8), main paper body) evaluated at $\beta = \widehat{\beta}$. The variance-covariance matrix $\widehat{V}_{WLS}$ is of dimension $P \times P$ and is a linear approximation of the inverse of the Hessian matrix of Φ_{Param}. Its graphical representation is an hyperelipsoid of dimension P known as Indifference Regions (IR). In this work, IR with a confidence level of 95% will be plotted.

With this approximation, the Confidence Interval (CI) for parameter $\widehat{\beta}$ is computed as [43]:

$$\beta_{p\,CI} = \widehat{\beta}_p \pm z_{\alpha/2}\sqrt{diag(\widehat{V}_{WLS})_p} \tag{14}$$

where $\widehat{\beta}_p$ is the pth element of $\widehat{\beta}$ and $z_{\alpha/2}$ is the cumulative distribution of a normally centered distribution function for a confidence level α.

Note that the particular residual error vector $e_{ij} = w_i u_{ij}$, which is the residual value for a specific noise copy ϵ_{ij}, is not taken into account to compute the variance-covariance matrix $\widehat{V}_{WLS}$ (equation (13)). The variances and associated weights w_i, taken into account while computing the Jacobian matrix F of $w_i\, Ln\left(B_{i\,SIM}(\beta,\theta)\right)$, must be properly estimated so that the calculated CIs are meaningful.

Input Noise Variance Evaluation

In this work, the variances σ_i^2 of the noise copies ϵ_{ij} (equation (7), main paper body) for each aperture diameter D_i were evaluated in two different ways.

Given equation (7) (main paper body), the classic way is to compare the experimental values $Ln\left(B_{ij\,EXP}\right)_k$ obtained on the phantom k, aperture diameter D_i and cycle j, with the averaged value $\overline{Ln\left(B_{ij\,EXP}\right)_k}$ over the number of cycles J_{ki} measured on the phantom k and with aperture diameter D_i, so that:

$$\sigma^2_{i\,Classic} = \frac{1}{(N_{ki}-K)}\sum_{k=1}^{K}\sum_{j}^{J_{ki}}\left(Ln\left(B_{ij\,EXP}\right)_k - \overline{Ln\left(B_{ij\,EXP}\right)_k}\right)^2 \tag{15}$$

where K is the number of phantoms, and J_{ki} is the total number of cycles for the phantom k and aperture diameter D_i. Thus, the parameter $N_{ki} = \sum_{k=1}^{K} J_{ki}$ is the number of tests that one has at hand for aperture diameter D_i.

The unbiased variance $\sigma^2_{i\,Classic}$ is an exact evaluation under the hypothesis that the model perfectly fits the data and that the random disturbance ϵ_{ij} is of zero mean: in equation (15), the average value $Ln\left(B_{ij\,EXP}\right)_k$ plays the role of a model that 'perfectly' fits the data.

In the cases where these hypotheses are not perfectly met, the classic variance underestimates the actual variance. Another variance estimation, also known as the Almost Unbiased Estimator (AUE), has been implemented based on [60]:

$$\sigma^2_{i\,AUE} = \frac{1}{N_{ki}}\sum_{k=1}^{K}\sum_{j}^{J_{ki}}\frac{u^2_{ij\,k}}{(1-\widehat{h}_{ij_k})} \tag{16}$$

where $u_{ij\,k}$ is the residual error vector obtained on phantom k, aperture diameter D_i and cycle j after fitting a model on all phantom k experimental data (one cost function ϕ_{param} per phantom k, (equation (8), main paper body). The leverages $\widehat{h}_{ij_k}$ are the diagonal values of the 'hat' matrix H_k of dimensions $J_{ki} \times J_{ki}$ defined for the kth non-linear model on the phantom k. The hat matrix H_k defined for non-linear models on phantom k writes [43]:

$$H_k = F_k\left(\widehat{\beta}\right)\left[F_k^T\left(\widehat{\beta}\right)F_k\left(\widehat{\beta}\right)\right]^{-1}F_k^T\left(\widehat{\beta}\right) \tag{17}$$

where $F_k\left(\widehat{\beta}\right)$ is the $J_{ki} \times P$ Jacobian matrix of $w_i\, Ln\left(B_{i\,SIM\,k}(\beta,\theta)\right)$ evaluated at $\beta = \widehat{\beta}$ on the phantom k.

In this contribution, the AUE variance was computed iteratively. The starting weights were chosen so that $w_i^2 = 1$ to define the function Φ_{Param} in equation (8), (main paper body). The residual error vector $u_{ij\,k}$ minimizing Φ_{Param} (equation (9), main paper body) was then computed and injected in equation (16) to provide a variance estimation $\sigma^2_{i\,AUE}$. This estimation has then been used to compute new weights ($w_i^2 = 1/\sigma^2_{i\,AUE}$) and a new iteration was performed. Iterations were performed until the convergence of $\sigma^2_{i\,AUE}$ (few iterations in practice).

Declarations

Conflicts of Interest The authors declare that they have no known competing financial interests or personal relationships that could have influenced the work reported in this article.

References

1. Payan Y (ed) (2012) Soft Tissue Biomechanical Modeling for Computer Assisted Surgery. Springer, Berlin
2. Budday S, Sommer G, Birkl C, Langkammer C, Haybaeck J, Kohnert J, Bauer M, Paulsen F, Steinmann P, Kuhl E et al (2017) Mechanical characterization of human brain tissue. Acta Biomater 48:319–340
3. Gao Z, Lister K, Desai JP (2010) Constitutive modeling of liver tissue: experiment and theory. Ann Biomed Eng 38(2):505–516
4. Girard E, Chagnon G, Gremen E, Calvez M, Masri C, Boutonnat J, Trilling B, Nottelet B (2019) Biomechanical behaviour of human bile duct wall and impact of cadaveric preservation processes. J Mech Behav Biomed Mater 98:291–300
5. Kumaraswamy N, Khatam H, Reece GP, Fingeret MC, Markey MK, Ravi-Chandar K (2017) Mechanical response of human female breast skin under uniaxial stretching. J Mech Behav Biomed Mater 74:164–175
6. Masri C, Chagnon G, Favier D, Sartelet H, Girard E (2018) Experimental characterization and constitutive modeling of the biomechanical behavior of male human urethral tissues validated by histological observations. Biomech Model Mechanobiol 17(4):939–950
7. Avazmohammadi R, Li DS, Leahy T, Shih E, Soares JS, Gorman JH, Gorman RC, Sacks MS (2018) An integrated inverse model-experimental approach to determine soft tissue three-dimensional constitutive parameters: application to post-infarcted myocardium. Biomech Model Mechanobiol 17(1):31–53
8. Diab M, Kumaraswamy N, Reece GP, Hanson SE, Fingeret MC, Markey MK, Ravi-Chandar K (2020) Characterization of human female breast and abdominal skin elasticity using a bulge test. J Mech Behav Biomed Mater 103
9. Tonge TK, Atlan LS, Voo LM, Nguyen TD (2013) Full-field bulge test for planar anisotropic tissues: Part i-experimental methods applied to human skin tissue. Acta Biomater 9(4):5913–5925
10. Cox MA, Driessen NJ, Boerboom RA, Bouten CV, Baaijens FP (2008) Mechanical characterization of anisotropic planar biological soft tissues using finite indentation: experimental feasibility. J Biomech 41(2):422–429
11. Samani A, Zubovits J, Plewes D (2007) Elastic moduli of normal and pathological human breast tissues: an inversion-technique-based investigation of 169 samples. Phys Med Biol 52(6):1565
12. Zhao R, Sider KL, Simmons CA (2011) Measurement of layer-specific mechanical properties in multilayered biomaterials by micropipette aspiration. Acta Biomater 7(3):1220–1227. https://doi.org/10.1016/j.actbio.2010.11.004
13. Gefen A, Margulies SS (2004) Are *in vivo* and in situ brain tissues mechanically similar? J Biomech 37(9):1339–1352
14. Kerdok AE, Ottensmeyer MP, Howe RD (2006) Effects of perfusion on the viscoelastic characteristics of liver. J Biomech 39(12):2221–2231
15. Ottensmeyer MP (2002) *In vivo* measurement of solid organ viscoelastic properties. Stud Health Technol Inform pp. 328–333
16. Elahi SA, Connesson N, Chagnon G, Payan Y (2019) In-vivo soft tissues mechanical characterization: Volume-based aspiration method validated on silicones. Exp Mech 59(2):251–261
17. Fougeron N, Rohan PY, Haering D, Rose JL, Bonnet X, Pillet H (2020) Combining freehand ultrasound-based indentation and inverse finite element modeling for the identification of hyperelastic material properties of thigh soft tissues. J Biomech Eng 142(9). https://doi.org/10.1115/1.4046444
18. Frauziols F, Chassagne F, Badel P, Navarro L, Molimard J, Curt N, Avril S (2016) *In vivo* identification of the passive mechanical properties of deep soft tissues in the human leg. Strain 52(5):400–411. https://doi.org/10.1111/str.12204
19. Ranger BJ, Moerman KM, Anthony BW, Herr HM (2023) Constitutive parameter identification of transtibial residual limb soft tissue using ultrasound indentation and shear wave elastography. J Mech Behav Biomed Mater 137:105541. https://doi.org/10.1016/j.jmbbm.2022.105541
20. Sengeh DM, Moerman KM, Petron A, Herr H (2016) Multi-material 3-d viscoelastic model of a transtibial residuum from in-vivo indentation and MRI data. J Mech Behav Biomed Mater 59:379–392. https://doi.org/10.1016/j.jmbbm.2016.02.020
21. Wei H, Liu X, Dai A, Li L, Li C, Wang S, Wang Z (2021) *In vivo* measurement of the mechanical properties of facial soft tissue using a bi-layer material model. Int J Appl Mech 13(03):2150034
22. Xu M, Yang J (2015) Human facial soft tissue thickness and mechanical properties: a literature review. In: International Design Engineering Technical Conferences and Computers and Information in Engineering Conference. Am Soc Mech Eng 57045: V01AT02A045
23. Diridollou S, Berson M, Vabre V, Black D, Karlsson B, Auriol F, Gregoire J, Yvon C, Vaillant L, Gall Y, Patat F (1998) An in vivo method for measuring the mechanical properties of the skin using ultrasound. Ultrasound Med Biol 24(2):215–224
24. Diridollou S, Patat F, Gens F, Vaillant L, Black D, Lagarde J, Gall Y, Berson M (2000) *In vivo* model of the mechanical properties of the human skin under suction. Skin Res Technol 6(4):214–221
25. Hendriks F, Dv Brokken, Van Eemeren J, Oomens C, Baaijens F, Horsten J (2003) A numerical-experimental method to characterize the non-linear mechanical behaviour of human skin. Skin Res Technol 9(3):274–283. https://doi.org/10.1016/j.medengphy.2005.07.001
26. Hendriks F, Brokken D, Oomens C, Bader D, Baaijens F (2006) The relative contributions of different skin layers to the mechanical behavior of human skin *in vivo* using suction experiments. Med Eng Phys 28(3):259–266. https://doi.org/10.1016/j.medengphy.2005.07.001
27. Badir S, Bajka M, Mazza E (2013) A novel procedure for the mechanical characterization of the uterine cervix during pregnancy. J Mech Behav Biomed Mater 27:143–153
28. Müller B, Elrod J, Pensalfini M, Hopf R, Distler O, Schiestl C, Mazza E (2018) A novel ultra-light suction device for mechanical characterization of skin. PLoS ONE 13(8)
29. Hollenstein M, Bugnard G, Joos R, Kropf S, Villiger P, Mazza E (2013) Towards laparoscopic tissue aspiration. Med Image Anal 17(8):1037–1045
30. Kauer M, Vuskovic V, Dual J, Székely G, Bajka M (2002) Inverse finite element characterization of soft tissues. Med Image Anal 6(3):275–287
31. Lakhani P, Dwivedi KK, Parashar A, Kumar N (2021) Non-invasive in vivo quantification of directional dependent variation in mechanical properties for human skin. Front Bioeng Biotechnol 9
32. Nava A, Mazza E, Furrer M, Villiger P, Reinhart W (2008) *In vivo* mechanical characterization of human liver. Med Image Anal 12(2):203–216
33. Röhrnbauer B, Betschart C, Perucchini D, Bajka M, Fink D, Maake C, Mazza E, Scheiner DA (2017) Measuring tissue displacement of the anterior vaginal wall using the novel aspiration technique *in vivo*. Sci Rep 7(1):1–7
34. Schiavone P, Chassat F, Boudou T, Promayon E, Valdivia F, Payan Y (2009) *In vivo* measurement of human brain elasticity using a light aspiration device. Med Image Anal 13(4):673–678
35. Vuskovic V (2001) Device for in-vivo measurement of mechanical properties of internal human soft tissues. PhD thesis, ETH Zurich
36. Weickenmeier J, Jabareen M, Mazza E (2015) Suction based mechanical characterization of superficial facial soft tissues. J Biomech 48(16):4279–4286
37. Luboz V, Promayon E, Payan Y (2014) Linear elastic properties of the facial soft tissues using an aspiration device: towards patient specific characterization. Ann Biomed Eng 42(11):2369–2378

38. Elahi SA, Connesson N, Payan Y (2018) Disposable system for in-vivo mechanical characterization of soft tissues based on volume measurement. J Mech Med Biol 18(04):1850037. https://doi.org/10.1142/S0219519418500379
39. Kappert K, Connesson N, Elahi S, Boonstra S, Balm A, van der Heijden F, Payan Y (2021) In-vivo tongue stiffness measured by aspiration: Resting vs general anesthesia. J Biomech 114
40. Barbarino GG, Jabareen M, Mazza E (2011) Experimental and numerical study on the mechanical behavior of the superficial layers of the face. Skin Res Technol 17(4):434–444. https://doi.org/10.1111/j.1600-0846.2011.00515.x
41. Sachs D, Wahlsten A, Kozerke S, Restivo G, Mazza E (2021) A biphasic multilayer computational model of human skin. Biomech Model Mechanobiol 20(3):969–982
42. MacKinnon JG (2013) Thirty years of heteroskedasticity-robust inference. In: Recent advances and future directions in causality, prediction, and specification analysis, Springer, pp 437–461
43. Sidik K, Jonkman JN (2016) A comparison of the variance estimation methods for heteroscedastic nonlinear models. Stat Med 35(26):4856–4874. https://doi.org/10.1002/sim.7024
44. Douglas MBates DGW (1988) Nonlinear Regression Analysis and Its Applications. John Wiley & Sons, Inc. https://doi.org/10.1002/9780470316757
45. Marquardt DW (1963) An algorithm for least-squares estimation of nonlinear parameters. J Soc Ind Appl Math 11(2):431–441
46. Shao J (1990) Asymptotic theory in heteroscedastic nonlinear models. Statist Probab Lett 10(1):77–85
47. Jemec G, Jemec B, Jemec B, Serup J (1990) The effect of superficial hydration on the mechanical properties of human skin *in vivo*: implications for plastic surgery. Plast Reconstr Surg 85(1):100–103
48. Park A (1972) Rheology of stratum corneum-i: A molecular interpretation of the stress-strain curve. J Soc Cosmet Chem 23:3–12
49. Joodaki H, Panzer MB (2018) Skin mechanical properties and modeling: A review. Proc Inst Mech Eng Part H: J Eng Med 232(4):323–343
50. Kalra A, Lowe A, Al-Jumaily A (2016) Mechanical behaviour of skin: a review. J Mater Sci Eng 5(4):1000254
51. Mostafavi Yazdi SJ, Baqersad J (2022) Mechanical modeling and characterization of human skin: A Rev J Biomech 130:110864
52. Mîra A, Carton AK, Muller S, Payan Y (2018) A biomechanical breast model evaluated with respect to mri data collected in three different positions. Clin Biomech Elsevier Ltd 60:191–199
53. Nazari MA, Perrier P, Chabanas M, Payan Y (2010) Simulation of dynamic orofacial movements using a constitutive law varying with muscle activation. Comput Methods Biomech Biomed Engin 13(4):469–482
54. Pensalfini M, Weickenmeier J, Rominger M, Santoprete R, Distler O, Mazza E (2018) Location-specific mechanical response and morphology of facial soft tissues. J Mech Behav Biomed Mater 78:108–115
55. Mukhina E, Rohan PY, Connesson N, Payan Y (2020) Calibration of the fat and muscle hyperelastic material parameters for the assessment of the internal tissue deformation in relation to pressure ulcer prevention. Comput Methods Biomech Biomed Engin 23(sup1):S197–S199. https://doi.org/10.1080/10255842.2020.1813426
56. Bucki M, Luboz V, Perrier A, Champion E, Diot B, Vuillerme N, Payan Y (2016) Clinical workflow for personalized foot pressure ulcer prevention. Med Eng Phys 38(9):845–853
57. Chinesta F, Cueto E (2015) Techniques de reduction de modeles vers une nouvelle generation d'abaques numeriques. Techniques de l'ingenieur Mathematiques base documentaire : TIP052WEB.(ref. article : af1381), 10.51257/a-v1-af1381, https://www.techniques-ingenieur.fr/base-documentaire/sciences-fondamentales-th8/analyse-numerique-des-equations-differentielles-et-aux-derivees-partielles-42620210/techniques-de-reduction-de-modeles-af1381/, fre,base documentaire : TIP052WEB
58. Aoki T, Ohashi T, Matsumoto T, Sato M (1997) The pipette aspiration applied to the local stiffness measurement of soft tissues. Ann Biomed Eng 25(3):581–587
59. Aversano G, Bellemans A, Li Z, Coussement A, Gicquel O, Parente A (2019) Application of reduced-order models based on pca & kriging for the development of digital twins of reacting flow applications. Computers & Chemical Engineering 121:422–441
60. Horn SD, Horn RA, Duncan DB (1975) Estimating heteroscedastic variances in linear models. Journal of the American Statistical Association 70(350):380–385, http://www.jstor.org/stable/2285827